Studies of the Collimator System
for the TTF Phase 2

V. Balandin, K. Flöttmann, N. Golubeva, and M. Körfer

Deutsches Elektronen-Synchrotron DESY, Hamburg

Contents

1 Introduction

The experience of the TTF phase I indicates that a protection system for the undulators is desirable [1], and this report contains the studies of the collimator system for the TESLA Test Facility phase 2 (TTF2). Due to limitations of available space it is proposed to place the TTF2 collimator system in the beam line with a dogleg of about $24.6\,m$ length, which, besides the collimation elements, has to contain the fast feedback system and to match the beam to the undulator entrance. So it was impossible to use the advantages of the popular spoiler-absorber scheme, and having only a limited number of available free positions, all proposed collimators are considered as primary collimators. Energy collimation and passive protection against off-energy bunches are achieved in the dogleg with horizontal dispersion.[1]

Basic parameters of the TTF phase 2 relevant to the problem in question are listed in table 1.

Table 1: TTF2 parameters

	Value	Symbol	Units
Energy	0.3 - 1.0	E_0	GeV
Bunch charge	1	Q	nC
Normalized emittance	2	ε_n	$mm \cdot mrad$
Bunch length, rms	50	σ_z	μm
Bunch energy spread	10^{-3}		
Repetition rate	10	f_t	Hz
Train duration	800	τ_t	μs
Bunch repetition rate	1 - 9	f_b	MHz
Maximum average power	72	P_{av}	kW

Besides studies of the specific questions related to the particular problems of the TTF2 collimator system, this report introduces two elements which seem to be of general importance: a new algorithm for the optimization of collimator apertures, and the optimal distance between collimator heat source and cooling water pipe, which reduces the maximal temperature of the collimator material.

---

[1]Note, that this dogleg is not designed specially for collimation purposes. It is included in the structure of the TTF2 linac for a later possible upgrade of the facility by installing additional undulators. But it is the only region with dispersion which can be used for collimation.

2 Protection Against Primary Particles

In the first step of our studies we have used the "black absorber" model for the collimators - any particle touching them is considered as lost. The purpose was to find the location of collimators and to determine the set of apertures which will stop all particles which would hit the undulators (**protecting apertures**). It is clear that only such apertures can be the subject of further studies which will take into account secondary particles and those rescattered into the beam.

Because of two strong sextupoles which where used in the dogleg for the correction of the second order dispersion and because of an unknown energy offset of halo particles from the nominal energy, it was not possible to limit the calculations to the linear non-chromatic optics only.

In addition to the undulator protection it is desirable to avoid uncontrolled losses (impacts) of the primary particles onto the beam pipe in the collimator section, which can lead to beam pipe damage if the whole beam is off-energy or (and) mis-steered.

2.1 Number and Location of Collimators

The requirement to provide beam parameters needed at the undulator entrance has first priority with respect to collimation. So, taking into account, that it is proposed to place the TTF2 collimator system in the beam line which contains the fast feedback system[2] and matches the beam to the undulator entrance, we face the problem to integrate the collimation elements into an almost fixed optics, rather than to create an optics most suitable for collimation. The energy collimation and passive protection against off-energy bunches can be achieved only in the region with dispersion, and thus we are forced to place one or two collimators in the dogleg. All remaining free places were looked over as candidates for location of additional (transverse) collimators, and as a result we consider two possible variants of collimator placement.

- **Scheme 1:** 1 collimator in the straight section before the dogleg (CT1); 2 collimators in the dogleg (CE1 and CE2); 1 collimator (CT2) in the

---

[2]Note, that a possible effect of the feedback kickers on the collimator system performance is not considered throughout this paper.
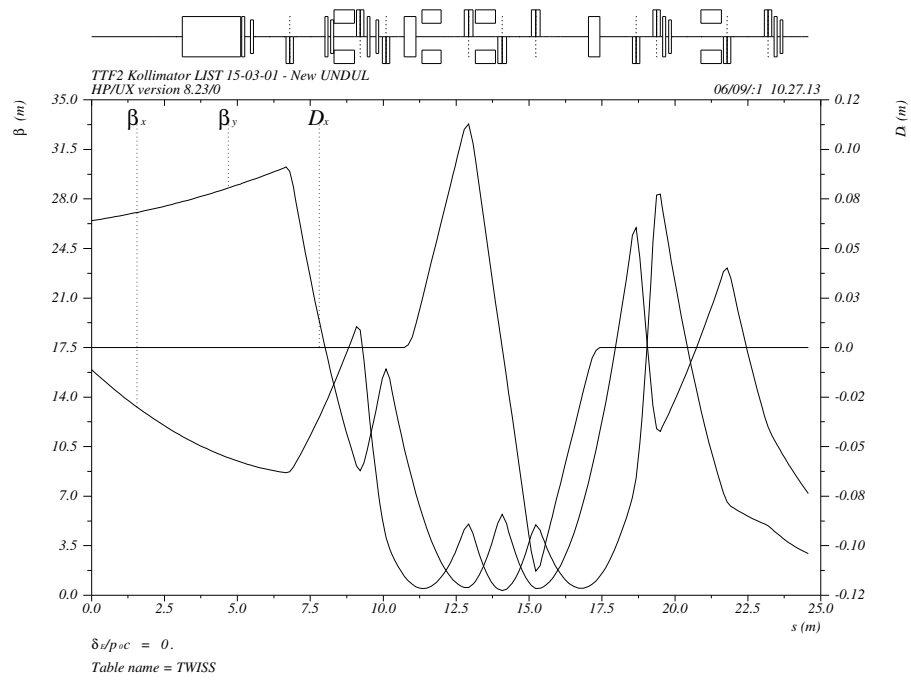
Figure 1: Optical functions of the TTF2 collimator section corresponding to the collimator location scheme 1.
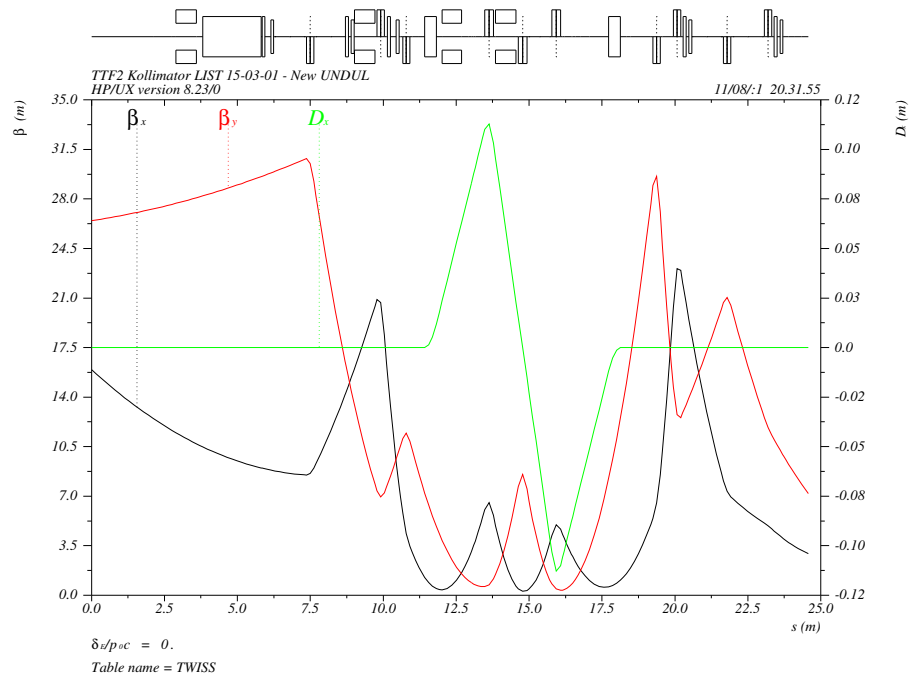
Figure 2: Optical functions of the TTF2 collimator section corresponding to the collimator location scheme 2.

straight section after the dogleg. Totally 4 collimators. Figure 1 shows the corresponding optical functions of the collimator section.

- **Scheme 2:** 2 collimators in the first straight part of the collimator section (CT1 and CT2); 2 collimators in the dogleg (CE1 and CE2). Totally 4 collimators. The corresponding optical functions, which are slightly different from the optical functions of the scheme 1, can be seen in figure 2.

2.2 Algorithm for the Optimization of Collimator Apertures

It looks hardly possible to describe the whole set of all kinds of protecting apertures constructively. However if we restrict ourselves to single particle dynamics (so collective effects and interaction of particles with the surrounding walls will be neglected), and to practically valuable apertures (for example, with elliptical or rectangular shape), it can be achieved quite easily. After choosing for each collimator the totally ordered scale of apertures (see details below), the distribution of the particles coming into the collimator section, and the particle tracking algorithm, it becomes possible to map the set of protecting apertures into a simply connected subset of the finite dimensional space. A special numerical procedure has been developed which allows us to find the borders of this subset and then to make some additional optimization within this subset, if necessary.

2.2.1 Totally Ordered Scale of Collimators

Let us define a collimator as a map $\mathcal{C}$, which either propagates a particle from position z_{en} in the beam line (collimator entrance) to position z_{ex} (collimator exit), or removes it from further consideration (absorbs the particle). So, having on the collimator entrance a set of incoming particles $\mathcal{P}_{en}$, we can find a set of particles $\mathcal{P}_{ex}$ which reaches the collimator exit without being absorbed with the help of the rule

$$\mathcal{C} : \mathcal{P}_{en} \to \mathcal{P}_{ex} .$$

Note that $\mathcal{P}_{ex}$ could be the empty set (all particles were absorbed).

Consider two collimators $\mathcal{C}_1$ and $\mathcal{C}_2$ which have the same entrance and exit locations. We write $\mathcal{C}_1 \le \mathcal{C}_2$ if for an arbitrary set $\mathcal{P}_{en}$ of incoming

particles $\mathcal{P}_{ex}^1 \subseteq \mathcal{P}_{ex}^2$. If, additionally, $\mathcal{P}_{ex}^1 \neq \mathcal{P}_{ex}^2$ at least for one set $\mathcal{P}_{en}$ of incoming particles, we say that $\mathcal{C}_1$ is smaller than $\mathcal{C}_2$ and write $\mathcal{C}_1 < \mathcal{C}_2$.

We say that the collimator $\mathcal{C}$ is a closed collimator and write $\mathcal{C} = 0$, if for an arbitrary set $\mathcal{P}_{en}$ of incoming particles, $\mathcal{P}_{ex}$ is the empty set ($\emptyset$).

A set $\{\mathcal{C}\}$ of collimators is totally ordered if all of them have the same entrance and exit locations and for each pair $\mathcal{C}_1, \mathcal{C}_2 \in \{\mathcal{C}\}$, at least one of the relations $\mathcal{C}_1 \leq \mathcal{C}_2$ or $\mathcal{C}_2 \leq \mathcal{C}_1$ is true.

Let R_+ be the set of all nonnegative real numbers. A totally ordered family of collimators $\{\mathcal{C}_r : r \in R_+\}$ is a totally ordered **scale of apertures** if $\mathcal{C}_0 = 0$ and $\mathcal{C}_{r_1} < \mathcal{C}_{r_2} \Leftrightarrow r_1 < r_2$.

2.2.2 Model of Single Pass Collimator System

Let us assume that we have fixed the number of collimators (n) and their locations, and have chosen for every collimator the totally ordered scale of apertures $\{\mathcal{C}_{r_i} : r_i \in R_+\}$, $i = 1, \ldots, n$. If, additionally, we fix the tracking algorithms $\mathcal{M}_{k,k+1}$, $k = 0, \ldots, n$ (the way how particles will be propagated through the beam line outside collimators), then the collimator system can be represented as a map

$$\mathcal{S}_\mathcal{C}\left(\vec{r}\right) = \mathcal{M}_{n,n+1} \circ \mathcal{C}_{r_n} \circ \mathcal{M}_{n-1,n} \circ \ldots \circ \mathcal{C}_{r_2} \circ \mathcal{M}_{1,2} \circ \mathcal{C}_{r_1} \circ \mathcal{M}_{0,1}. \tag{1}$$

To complete a description, we need to define the set of the particles coming into the beam line $\mathcal{P}_i$, and the target $\mathcal{T}$, which we hope to protect with the help of our collimator section.

For fixed apertures $\vec{r}$, we can find the set of particles which reaches the exit of our collimator system without being absorbed $\mathcal{P}_f\left(\vec{r}\right)$ with the help of the rule

$$\mathcal{S}_\mathcal{C}\left(\vec{r}\right) : \mathcal{P}_i \rightarrow \mathcal{P}_f\left(\vec{r}\right).$$

We say that the apertures $\vec{r} = (r_1, \ldots, r_n)$ are target protecting apertures, if

$$\mathcal{P}_f\left(\vec{r}\right) \bigcap \mathcal{T} = \emptyset.$$

We will denote the set of all protecting apertures[3] as $\mathcal{A} \subseteq R_+^n$, and will

---

[3]Sometimes it is useful to treat the maps $\mathcal{M}_{k,k+1}$ in (1) as fixed aperture collimators and add some properties of the set of absorbed particles to the definition of protecting apertures. Such generalizations are quite obvious and allow us, for example, to include the requirement to have no uncontrolled impacts of primary particles on the beam pipe between the collimators.

say that a set of protecting apertures $\mathcal{A}$ is nontrivial, if there exist a vector $\vec{r} \in \mathcal{A}$ such that $r_i \neq 0$ for all $i = 1, \ldots, n$.

2.2.3 Properties of the Set of Protecting Apertures

It is easy to check that the set of protecting apertures $\mathcal{A}$ introduced above admits the following properties

- If $\vec{r} \geq \vec{0}$ is such that at least one of its coordinates
  is equal to zero, then $\vec{r} \in \mathcal{A}$. In particular, $\vec{0} \in \mathcal{A}$.

- If $\vec{r}_* \in \mathcal{A}$, and $\vec{0} \leq \vec{r} \leq \vec{r}_*$, then $\vec{r} \in \mathcal{A}$.

- If $\vec{r}_* \in R_+^n \setminus \mathcal{A}$, and $\vec{r} \geq \vec{r}_*$, then $\vec{r} \in R_+^n \setminus \mathcal{A}$.

From this it follows, that if $\mathcal{A}$ is nontrivial, then the set $int(\mathcal{A})$ (interior of $\mathcal{A}$) is a simply connected set, and any line connecting the points $\vec{0}$ and $\vec{r} \in R_+^n \setminus \mathcal{A}$ intersects the bound of $int(\mathcal{A})$ in not more than one point different from $\vec{0}$.

Let $Q^n(L)$ be the n-dimensional cube with edge $L > 0$. Due to the properties of the set $int(\mathcal{A})$ mentioned above, the bound of the set $int(\mathcal{A}) \cap Q^n(L)$ can be found with any needed precision as a solution of a series of one-dimensional problems (for example, we can simply choose the set of rays starting from point $\vec{0}$, and then move along each ray until particles start to hit our target or we will reach the cube boundary), and then we can make some additional optimization within this set, if necessary.

2.2.4 Maximization of Minimal Aperture and Reference Solution

Let us consider as an optimization criteria the requirement to maximize the minimal aperture ($\min r_i \to \max$) within the closure of the set $int(\mathcal{A})$.

It can be shown, that a solution of this problem exists, but if we have more than one collimator, it can be not unique. One solution (which we will call the **reference solution**) can be always obtained by moving from the origin of the coordinate system along the ray $r_1 = r_2 = \ldots = r_n$ until particles start to hit our target. If this solution is not the only one which maximizes the minimal aperture, then the number of solutions is infinite and, of course, not all of them are equally interesting.

We will say that a solution $\vec{r}^1$ is dominated by another solution $\vec{r}^2$ if $\forall i \quad r_i^1 \leq r_i^2$ and $\exists i$ such that $r_i^1 < r_i^2$. If there is no other solution

10

$\vec{r}^2$ such that $\vec{r}^2$ dominates $\vec{r}^1$, then the solution $\vec{r}^1$ is said to be **non-dominated**.[4] All non-dominated solutions of our problem can be found by using the following iterative procedure: fix one coordinate in the reference solution and then find the reference solution of the problem with the one unit smaller dimension. Thus we can find $n!$ non-dominated solutions which maximize the minimal aperture, but some of them (or even all) can coincide.

Note, that every solution, which maximizes the minimal aperture, must have at least one collimator with the same aperture as in the reference solution.

Figure 3 shows us the reference solutions for the scheme 2 of locating collimators corresponding to six different chosen scales of apertures. In these calculations the collimator holes were considered as cylinders with elliptical or rectangular base and length of $0.4\,m$. Below one can find additional comments to figure 3, which describe the chosen scales of apertures.

- Line 1: Circular apertures for all four collimators with radii r_i.

- Line 2: Elliptical apertures with half-axes

$$r_x = r_i, \quad r_y = \frac{\sigma^i_y}{\sigma^i_x} \cdot r_i,$$

  where σ^i_y and σ^i_x are the beam sigmas in the places of the collimator locations.

- Line 3: Circular apertures with radii $\min(\sigma^i_y, \sigma^i_x) \cdot r_i$.

- Line 4: Elliptical apertures with half-axes

$$r_x = \sigma^i_x \cdot r_i \quad \text{and} \quad r_y = \sigma^i_y \cdot r_i.$$

- Line 5: Square apertures for all four collimators with half-sizes r_i.

- Line 6: Rectangular apertures with half-sizes

$$r_x = r_i, \quad r_y = \frac{\sigma^i_y}{\sigma^i_x} \cdot r_i.$$

---

[4]It is clear that the concept of dominance is important not only for the problem of maximization of the minimal aperture, but for any other optimization criterion. In the theory of multiobjective optimization the non-dominated solutions are also called Pareto optimal.

Figure 3 gives us a first feeling, what size of the collimator apertures we will obtain, if, after fixing the shape of the inner collimating tube, we will try to maximize their size in the real dimensions (lines 1, 2, 5, and 6), or in the units of beam sigmas (lines 3 and 4). Note, that the shown results were obtained for an energy deviation range of $-15\% \leq \Delta E/E_0 \leq 15\%$, and a safety factor for the undulator was $s_f = 0.9$. All other details, about the distribution of the particles coming into the collimator section, and about the particle tracking algorithm can be found in the following subsection.

2.3   Choice of Collimator Apertures

Based on considerations similar to those shown in figure 3, we chose circular holes as the shape of the inner collimating tube, and in this subsection we will describe in detail the result of the optimization of their sizes in real dimensions (not in units of beam sigmas).

2.3.1   Distribution of Incoming Particles

Because the distribution of the incoming particles, which need to be collimated, is difficult to predict precisely (it depends on how well the upstream system has been tuned, on emission of dark current, and so on) the initial distribution was modeled by 4-dimensional slices $(x,\ p_x,\ y,\ p_y)$, with a transverse extent over the radius of the vacuum chamber at the collimator section entrance (the maximum values for momentums p_x and p_y were chosen so as to fully populate the acceptance of the transport line), and with the same value of energy deviation $\Delta E/E_0$ for all particles in each slice (monochromatic $\Delta E/E_0$ - fractions). The number of particles in each slice was chosen to be $2 \cdot 10^5$. The optimization procedure described above was performed for each slice separately and the results are presented as a function of the energy deviation $\Delta E/E_0$.

2.3.2   Particle Tracking Algorithm

As particle tracking algorithm the symplectic numerical integration of the exact Hamiltonian equations of motion in the SCOFF approximation was used (thus geometrical and chromatic aberrations were taken into account, but possible effects of fringe fields were not included).

Figure 3: Reference solutions corresponding to six different chosen scales of apertures. Collimator location scheme 2.

2.3.3 Criteria for Undulator to be Protected

Particles which safely passed the collimator section were tracked further through the undulator and if even one of them was able to touch the undulator aperture (reduced by $s_f = 0.9$ times), then a protection failure was recorded.

In part of the calculations we have used an additional requirement to avoid losses (impacts) of the particles on the beam pipe between the collimators (**uncontrolled losses**).

2.3.4 Results for Collimator Location Scheme 2

Figure 4 shows the resulting maximized minimal aperture radius (**reference solution radius**)[5] in the energy deviation range of $-50\% \leq \Delta E/E_0 \leq +25\%$. The minimum value of $\sim 2\,mm$, seen in figure 4, means that at least one collimator must stay within such an aperture radius. With a careful additional search for non-dominated solutions, which maximize the minimal aperture, it was found that 3 collimators must keep this value as aperture radius and the radius of the first energy collimator (placed just after the first dipole magnet in the dogleg) can be safely increased to $6 - 7\,mm$ (see figure 5).

Besides the calculation of the undulator protecting apertures, it was interesting to find apertures which, for a given energy offset $\Delta E/E_0$, will stop the corresponding $\Delta E/E_0$-fraction of the incoming particles in the collimator section completely.

The result of these investigations is plotted in figure 6, and one can see that in the region $|\Delta E/E_0| > 3\%$ the presented graphs coincides with the corresponding curves seen in figure 4. This means that for $|\Delta E/E_0| > 3\%$ in each monochromatic fraction of the initial distribution particles with arbitrarily small transverse positions x and y at the entrance of the collimator system would, nevertheless, hit the undulator vacuum chamber (of course, in the absence of the collimators). At first sight one may conclude that this is the result of a large undumped nonlinear dispersion. But more detailed tracking calculations show us that the residual nonlinear dispersion, if taken alone, is not large enough to cause this effect (see figure 7). Rather it can be

---

[5]Note that, in fact, this and the following figures show not the reference solution radius, but the minimum of this radius and the maximal radius of the vacuum chamber in the collimator section $(0.022\,m)$.
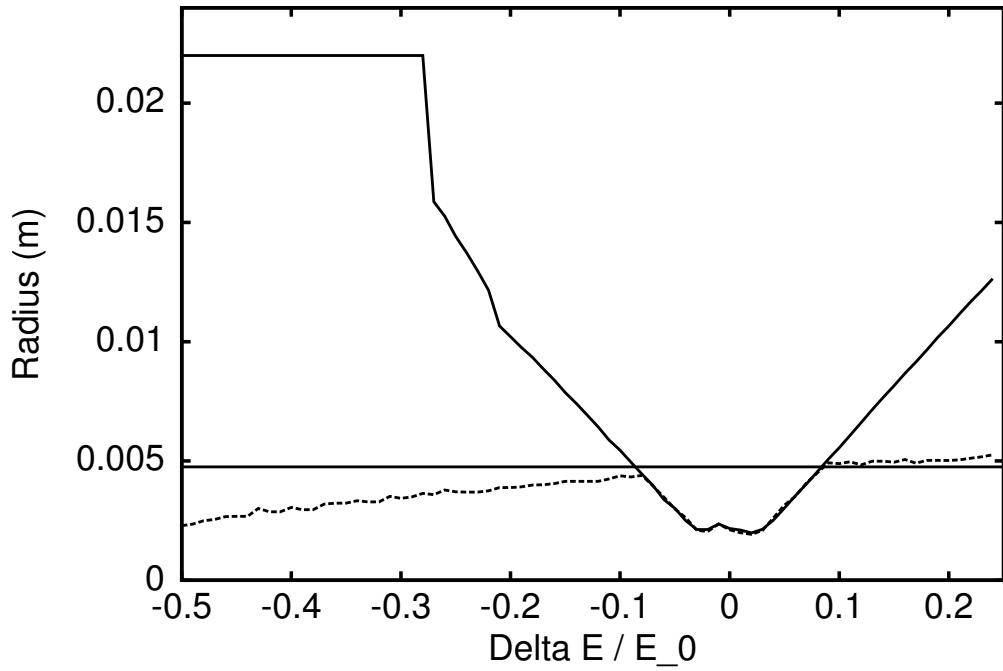
Figure 4: Solid curve: reference solution radius as a function of the energy deviation. Dashed curve: with additional requirement to have no uncontrolled losses in the collimator section. The horizontal straight line shows the undulator aperture. Collimator location scheme 2.
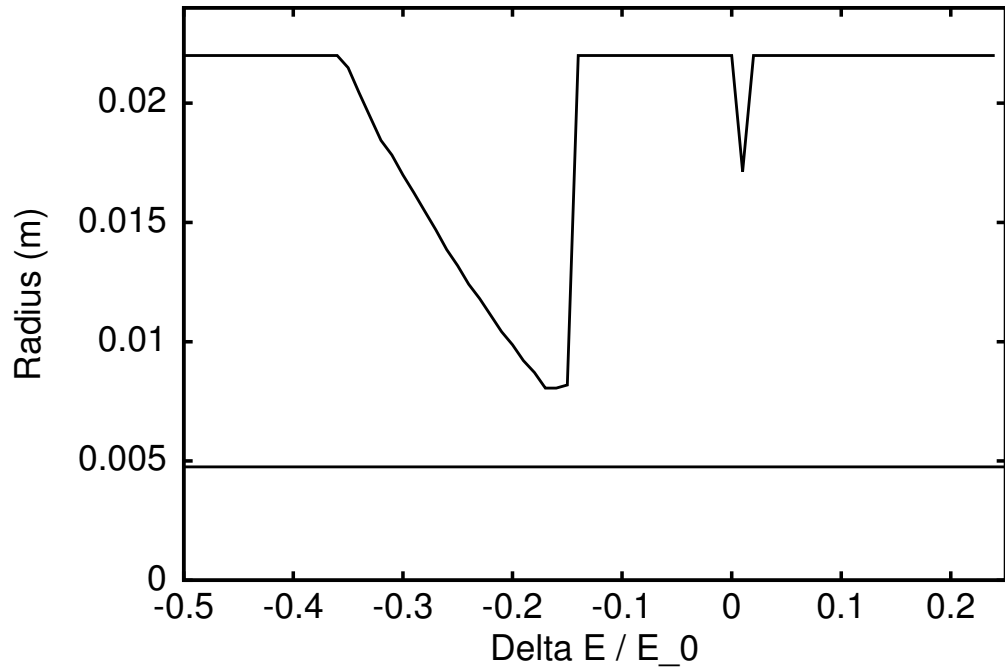
Figure 5: Aperture radius of the CE1 collimator as a function of the energy deviation. The remaining collimators have aperture radii $2\,mm$. There are no uncontrolled losses in the collimator section. The horizontal straight line shows the undulator aperture. Collimator location scheme 2.

Figure 6: Solid curve: aperture radius required to block the corresponding $\Delta E/E_0$-fractions of incoming particles in the collimator section. Dashed curve: with additional requirement to have no uncontrolled losses in the collimator section. The horizontal straight line shows the undulator aperture. Collimator location scheme 2. All four collimators are assumed to have the same aperture radius.
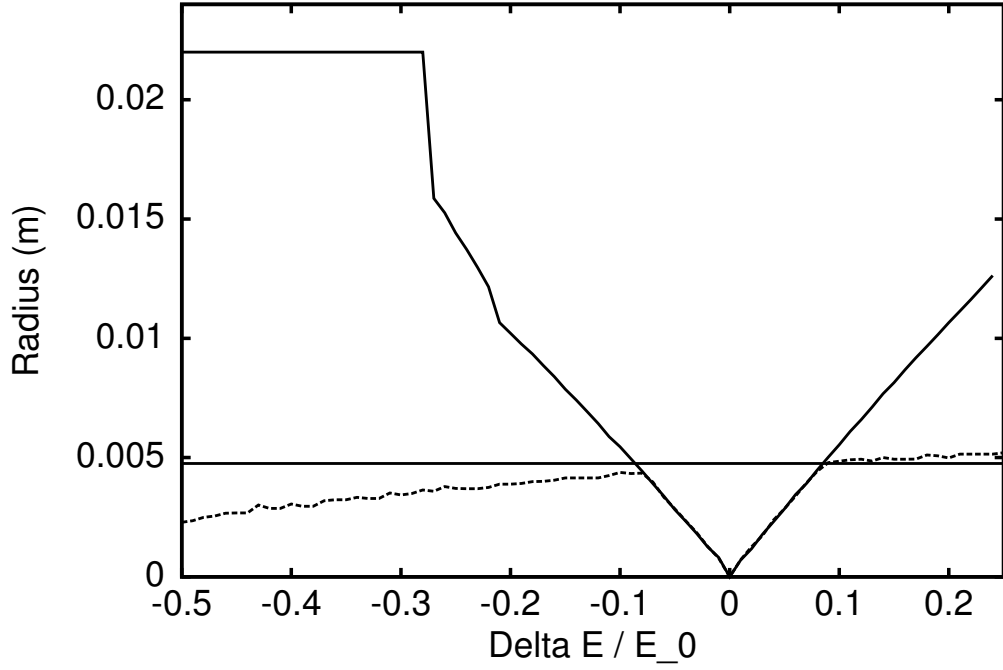
considered as the result of the interaction of the energy offset with the initial nonzero vertical momentum, and this interaction is produced by the strong sextupoles (compare figures 7 and 8).

Recommended apertures radii:

- r(CT1) = r(CT2) = r(CE2) = $2\,mm$, and r(CE1) = $6\,mm$.

These apertures allows us to protect both, the undulator and the beam pipe in the collimator section.

2.3.5   Results for Collimator Location Scheme 1

In the collimator location scheme 1 the phase advances in both planes between first and last collimators (CT1 and CT2) are very close to multiple of 90°. So, if we will neglect uncontrolled losses on the beam pipe between the collimators, the maximized minimal aperture radius can be increased up to $\sim 3.2\,mm$ (see figure 9). But, in order to avoid these losses, one needs to reduce the aperture radius to $\sim 1\,mm$ (further studies have shown that this reduction can be done for two energy collimators only).

Recommended apertures radii:

If we will take care about undulator protection only, then we can choose

- r(CT1) = r(CT2) = r(CE2) = $3.2\,mm$, and r(CE1) = $6\,mm$.

In this case losses on the beam pipe in the collimator section can be seen in figure 10. In the following mentioning scheme 1 we will have in mind this apertures only, because if we would like to protect additionally the beam pipe, then we have to choose between the following two solutions[6]

- r(CT1) = r(CT2) = $3.2\,mm$, r(CE1) = r(CE2) = $1.2\,mm$,

- r(CT1) = r(CT2) = r(CE2) = $3.2\,mm$, r(CE1) = $1.0\,mm$,

which looks unpractical.

---

[6]The first solution maximizes the minimal aperture, and the second maximizes the sum of apertures within the intersection of the set of protecting apertures and the set $\{\vec{r} : r_i \geq 1.0\,mm, i = 1, 2, 3, 4.\}$.

Figure 7: Trajectories of four particles along the TTF2 collimator section and undulators. The entrance of the first undulator is located at a distance of $24.6\,m$. Transverse initial conditions are $x^0 = p_x^0 = y^0 = p_y^0 = 0$, and energy offsets are $\Delta E/E_0 = -2\%,\ -4\%,\ -6\%,\ -8\%$.
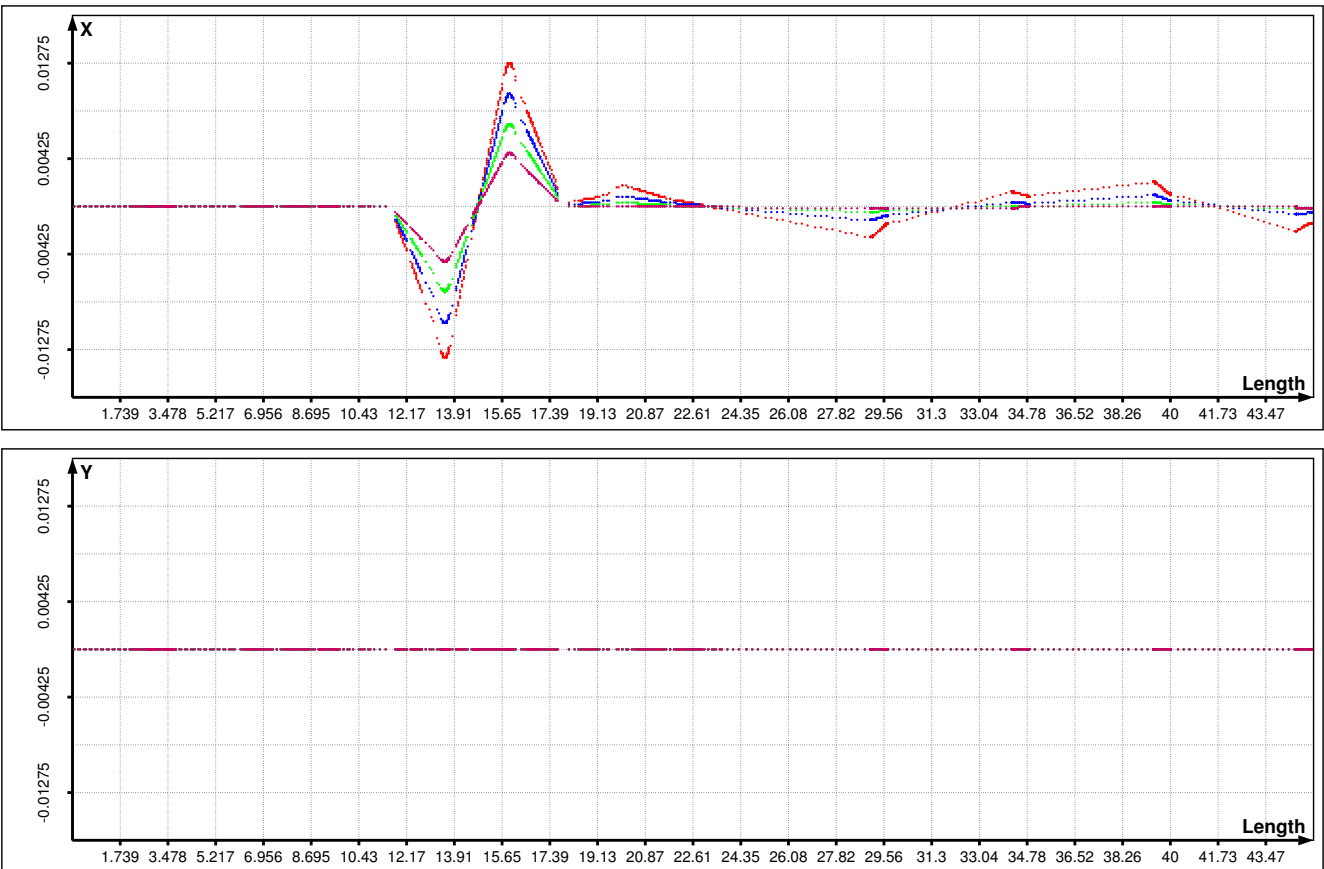
19
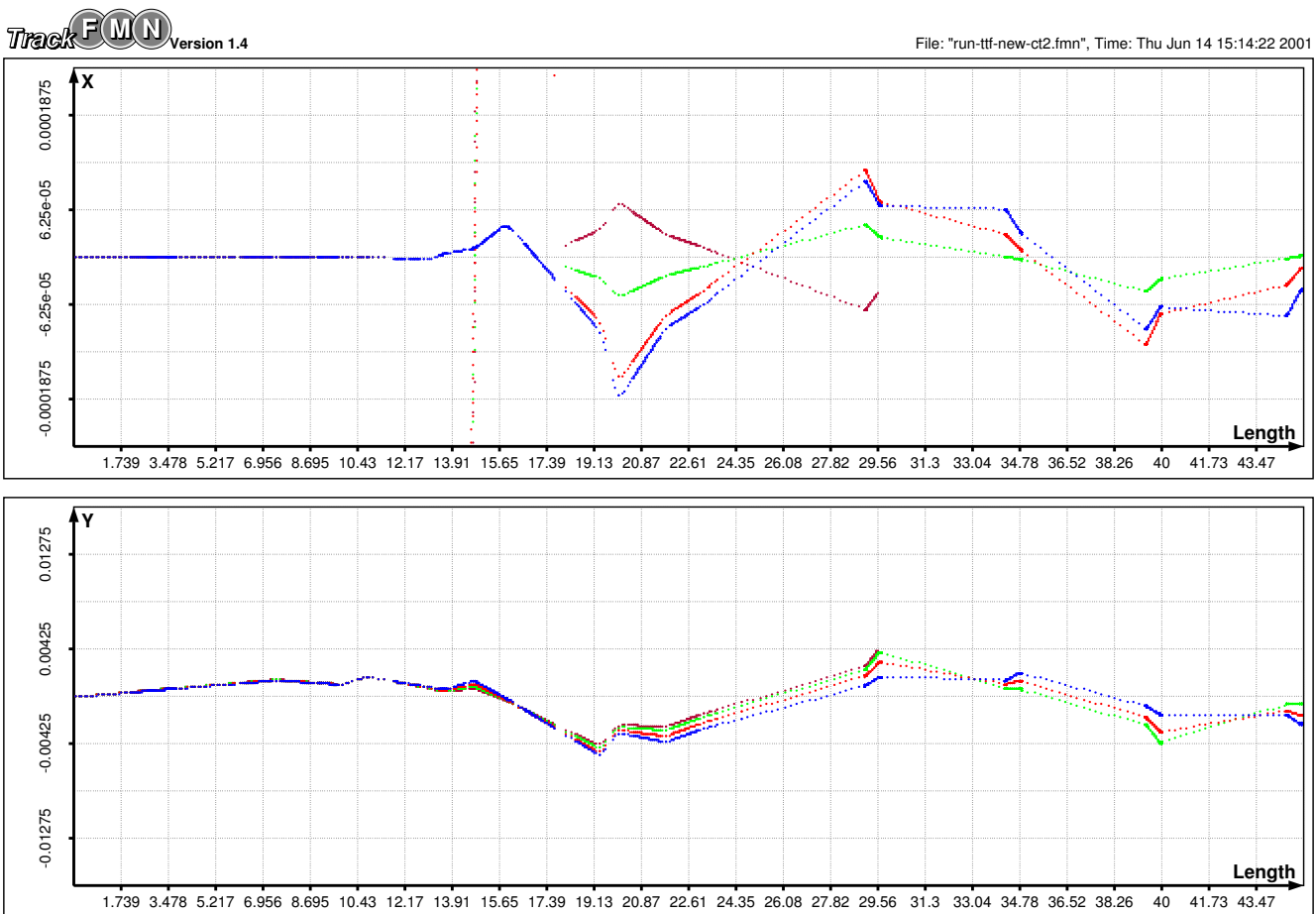
Figure 8: Trajectories of four particles along the TTF2 collimator section and undulators. The entrance of the first undulator is located at a distance of $24.6\,m$. Transverse initial conditions are $x^0 = p_x^0 = y^0 = 0$, $p_y^0 = 2 \cdot 10^{-4}$, and energy offsets are $\Delta E/E_0 = 0\%$, -2.2%, -4%, -5%.
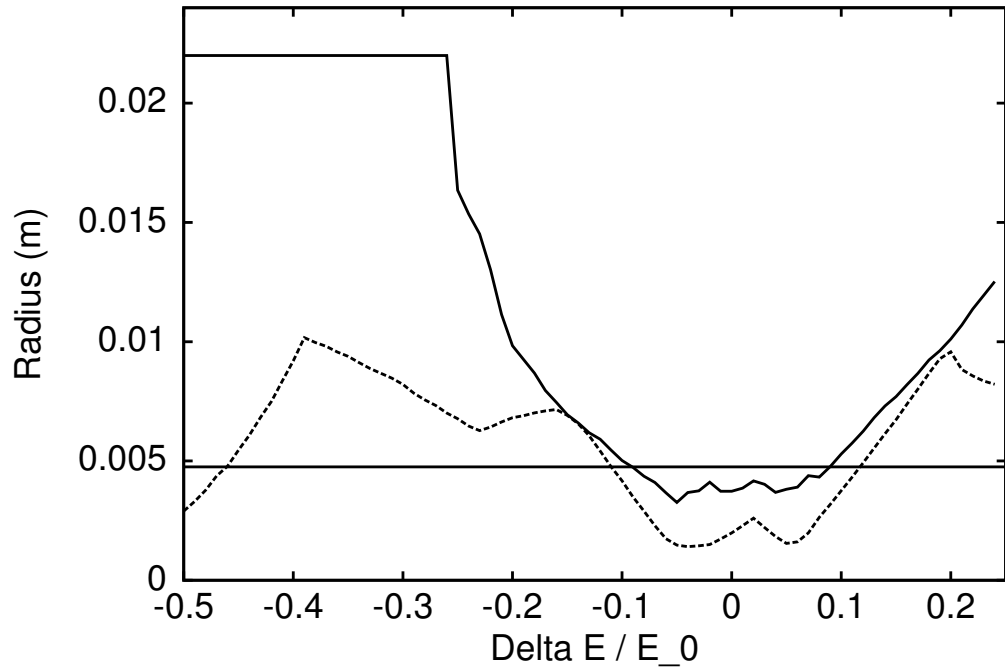
Figure 9: Solid curve: reference solution radius as a function of the energy deviation. Dashed curve: with additional requirement to have no uncontrolled losses in the collimator section. The horizontal straight line shows the undulator aperture. Collimator location scheme 1.

Figure 10: Uncontrolled losses in the collimator section (% of incoming parti-
cles). Collimator location scheme 1. $r(CT1) = r(CT2) = r(CE2) = 3.2\,mm$,
and $r(CE1) = 6\,mm$.

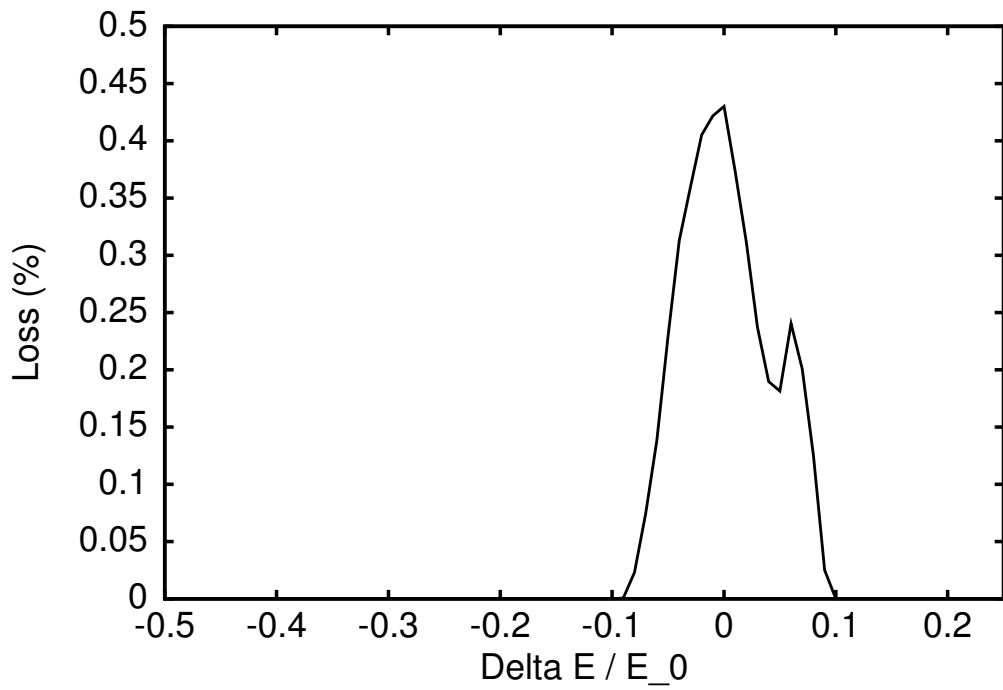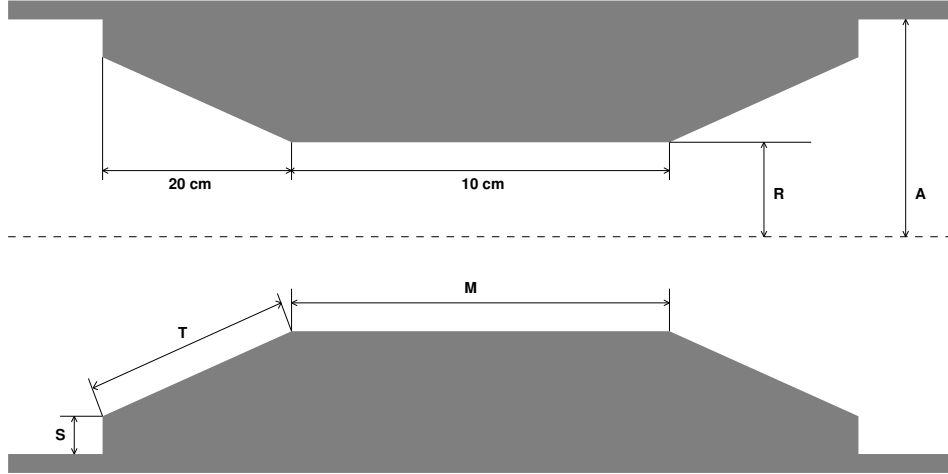Figure 11: Collimator geometry (not in scale).

2.4   Length of Collimators

The above described optimization has been performed for a variety of lengths of the collimators[7], and this study has shown us that the dependence of the optimized apertures on the collimator length is relatively weak. For example, reducing the length from $70\,cm$ to $20\,cm$ decreases the value of the reference solution radius by $\sim 7\%$ only. But let us remind, that these calculations were done considering the collimators as black absorbers. In reality, when particles hit a collimator surface, they and (or) the generated secondaries can be scattered back into the collimating tube instead of being absorbed. These particles will be either removed at a later part of the collimator or scattered into the collimating tube again. From this point of view it is preferable to have long collimators.

Being limited by the available space, we chose the total length of the collimator[8] equal to $50\,cm$ including the tapers on both sides to reduce the wakefield effects. The length of each taper is $20\,cm$ [2], so the main part of the collimator (the part, which is parallel to the beam line axis) is $10\,cm$, see figure 11 and table 2.

---

[7]Generally speaking, one has to distinguish the length of the collimator and the length of its inner collimating tube, but, because we do not consider throughout this paper any details of the mechanical design of the collimators, they are assumed to be equal.

[8]To simplify the hardware design, all four collimators have the same length.

Table 2: Parameters of collimator geometries

Scheme 1					
	A, m	R, m	S, m	T, m	M, m
CT1	0.017	0.0032	0.0115	0.2000132	0.100
CE1	0.022	0.0060	0.0140	0.2000100	0.100
CE2	0.022	0.0032	0.0165	0.2000132	0.100
CT2	0.017	0.0032	0.0115	0.2000132	0.100
Scheme 2					
CT1	0.017	0.0020	0.0125	0.2000156	0.100
CT2	0.017	0.0020	0.0125	0.2000156	0.100
CE1	0.022	0.0060	0.0140	0.2000100	0.100
CE2	0.022	0.0020	0.0170	0.2000225	0.100

3   Advanced Tracking Studies with Primary Particles

After fixing the collimator geometries (see figure 11 and table 2) additional tracking simulations were performed to answer the questions: How are the lost primary particles distributed between the four collimators and along the surface of collimators; what are the maximum and average angles at which a primary particles hit the surface of the collimators; which monochromatic $\Delta E/E_0$ - fractions of the incoming particles will be stopped by the collimator system completely?

3.1   Results for Collimator Location Scheme 1

All particles with an energy offset $|\Delta E/E_0| > 6\%$ will be stopped in the collimator section completely (at this point of our investigation, of course, in the black absorber model for the collimators).

Figures 12, 13, 14, and 15 show the distribution of losses (impacts) of primary particles integrated over the azimuthal angle along the collimator surfaces as a function of the energy deviation.[9]

We see in figure 15 that most of the captured particles are intercepted by the entrance step and the entrance taper, and only less than 1% of all particles absorbed by CT2 collimator (last collimator for the scheme 1) hit the main part of this collimator.

Note, that losses on beam pipe between collimators for the tapered collimators are similar to those presented in figure 10.

3.2   Results for Collimator Location Scheme 2

All particles with an energy offset $|\Delta E/E_0| > 3\%$ will be stopped in the collimator section completely.

Figures 16, 17, 18, and 19 show the distribution of losses of primary particles integrated over the azimuthal angle along the collimator surfaces as a function of the energy deviation.

---

[9]The collimator surface consist of five parts: the entrance step, the entrance taper, the main part (the part, which is parallel to the beam line axis), the exit taper, and the exit step (S-T-M-T-S in figure 11), and the corresponding colors in the distribution plots are: red, green, red, green, and red again.

Figure 12: Distribution of lost primary particles integrated over the azimuthal angle along the collimator surface as a function of the energy deviation. Collimator CT1. Collimator location scheme 1.

Similar to the scheme 1 we see in figure 19 that again less than 1% of all particles absorbed by the CE2 collimator (last collimator for the scheme 2) hit its main part.

Figure 13: Distribution of lost primary particles integrated over the azimuthal angle along the collimator surface as a function of the energy deviation. Collimator CE1. Collimator location scheme 1.

Figure 14: Distribution of lost primary particles integrated over the azimuthal angle along the collimator surface as a function of the energy deviation. Collimator CE2. Collimator location scheme 1.

Figure 15: Distribution of lost primary particles integrated over the azimuthal angle along the collimator surface as a function of the energy deviation. Collimator CT2. Collimator location scheme 1.
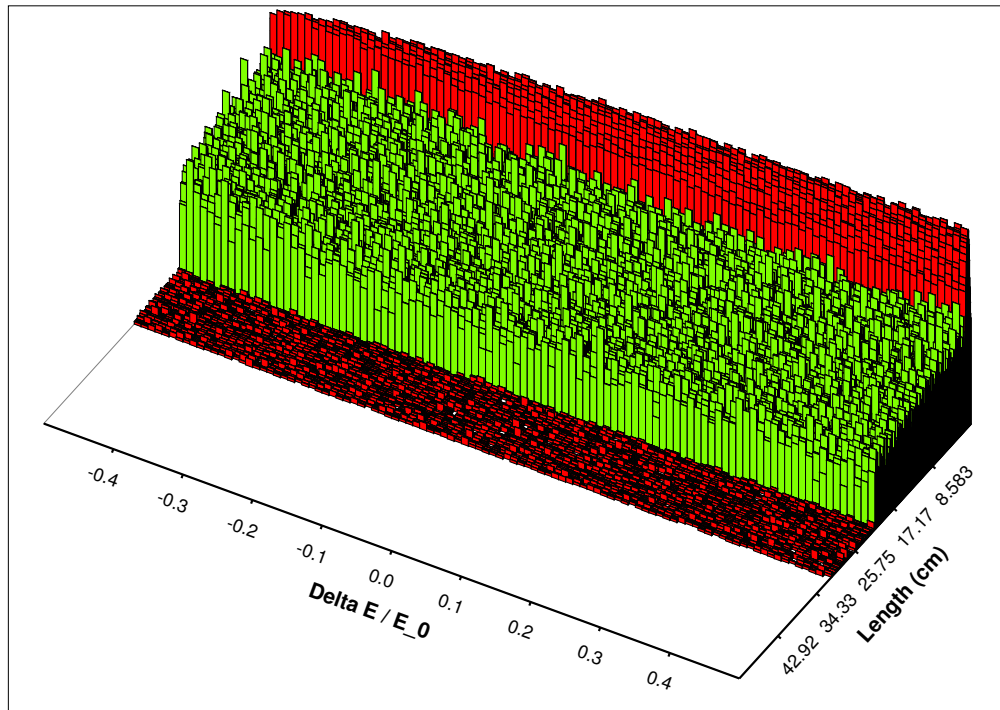
Figure 16: Distribution of lost primary particles integrated over the azimuthal angle along the collimator surface as a function of the energy deviation. Collimator CT1. Collimator location scheme 2.

Figure 17: Distribution of lost primary particles integrated over the azimuthal angle along the collimator surface as a function of the energy deviation. Collimator CT2. Collimator location scheme 2.
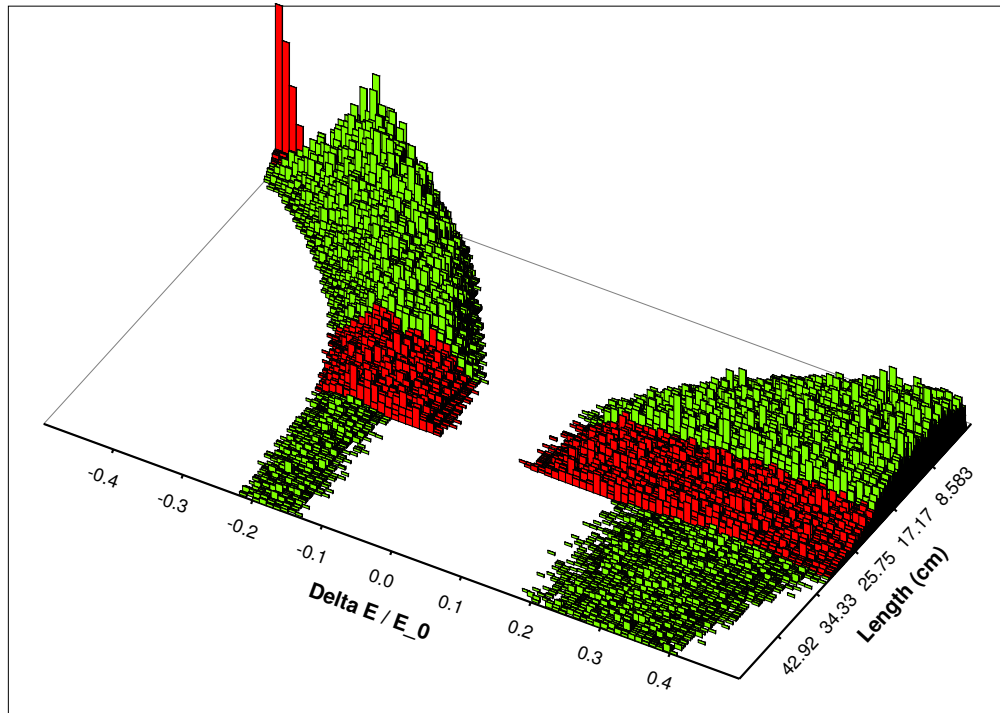
31

Figure 18: Distribution of lost primary particles integrated over the azimuthal angle along the collimator surface as a function of the energy deviation. Collimator CE1. Collimator location scheme 2.
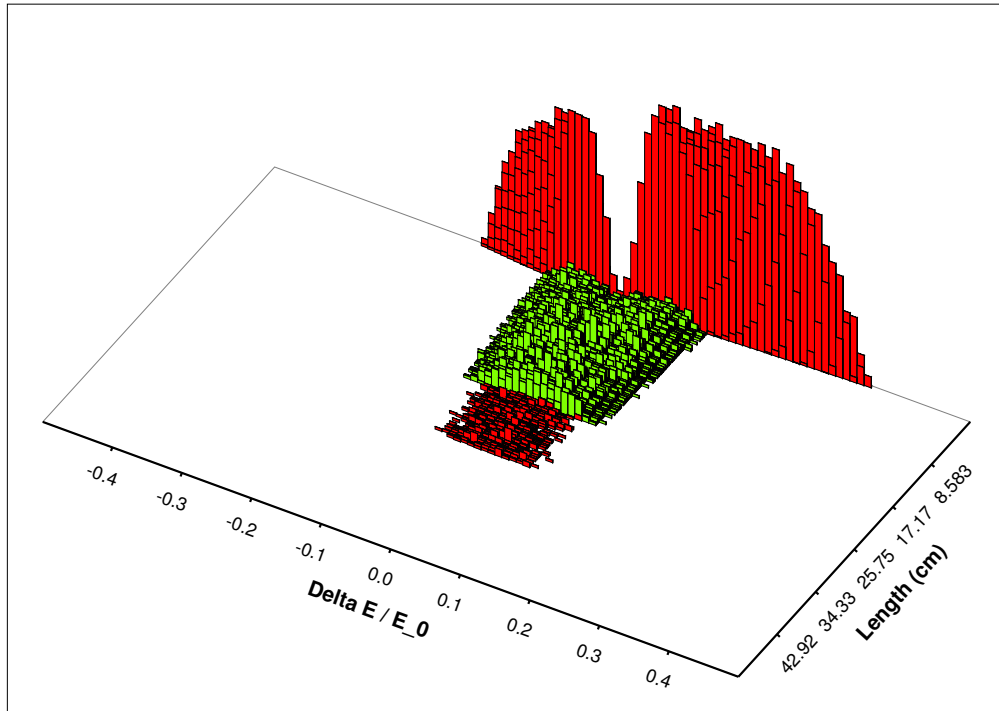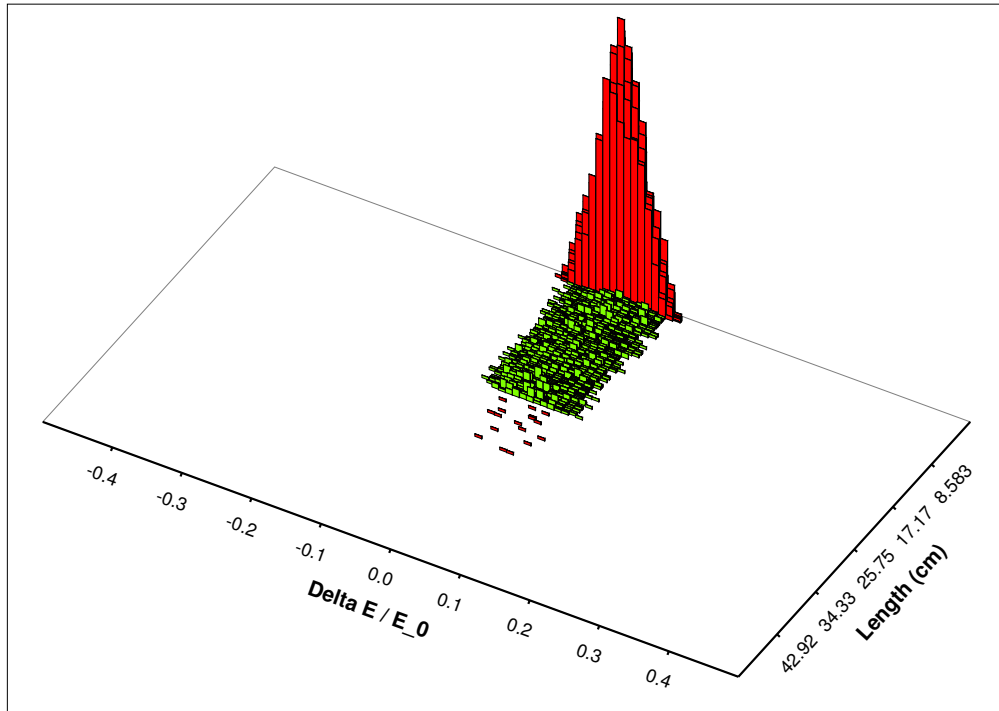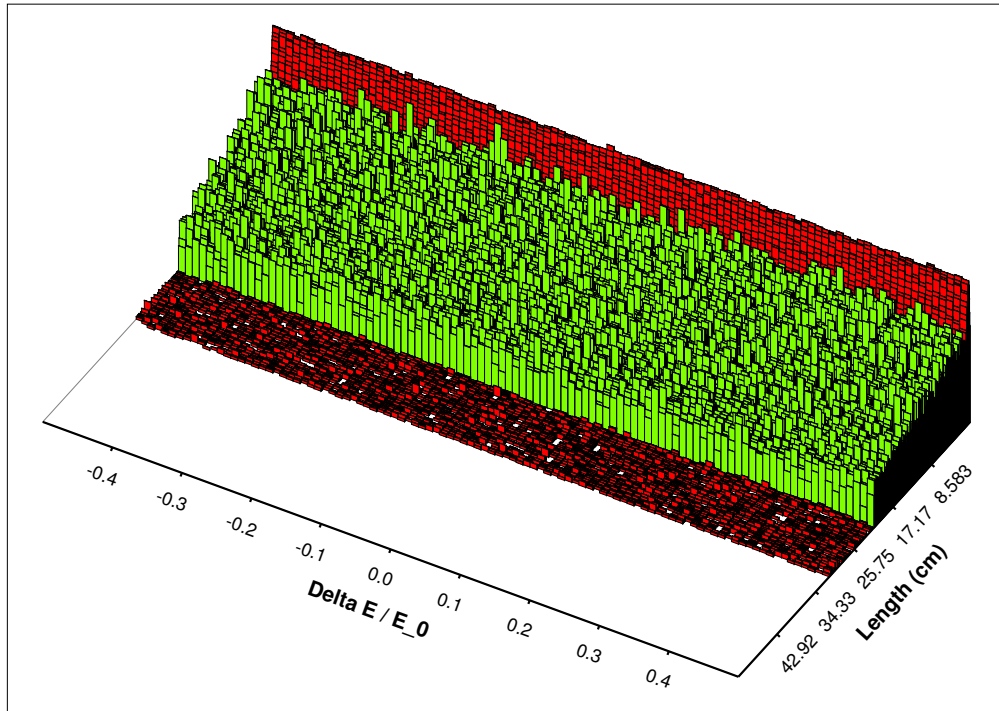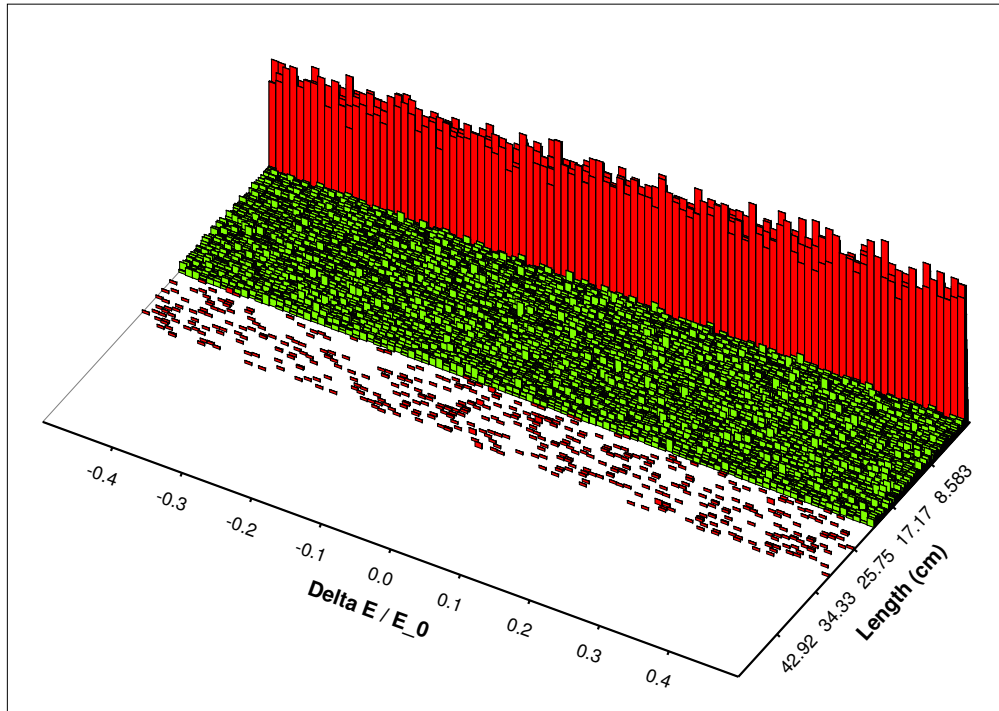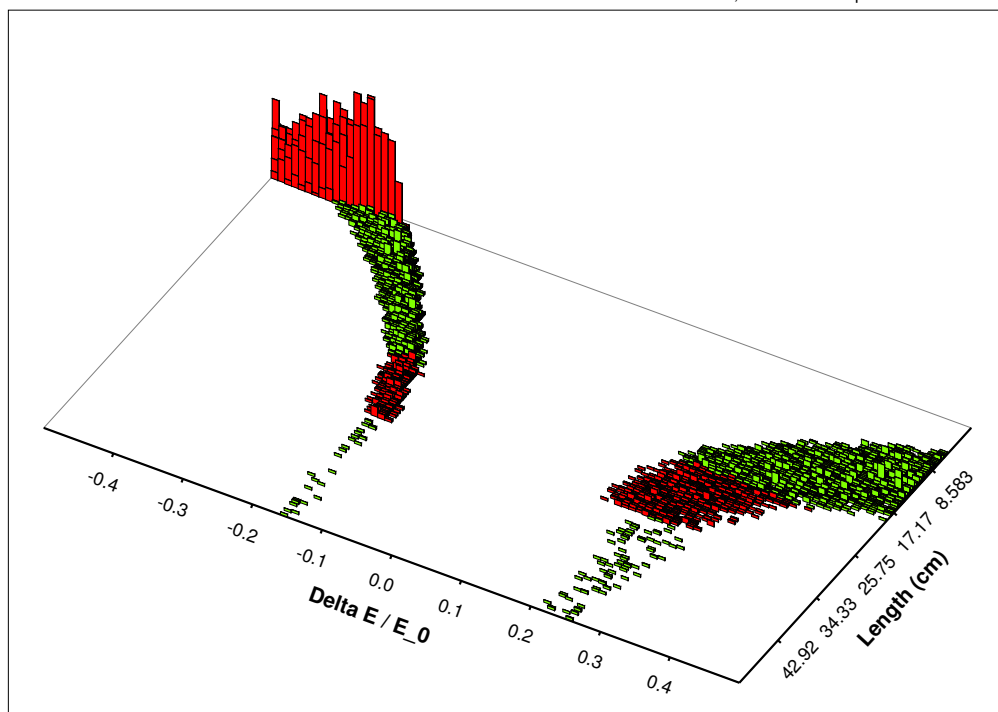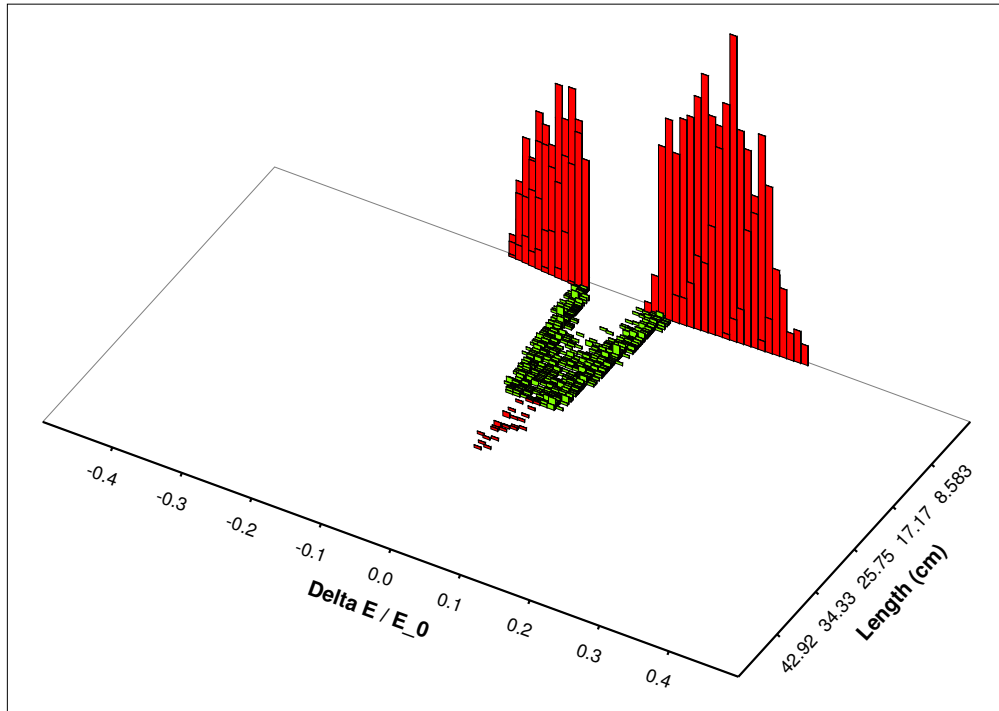
Figure 19: Distribution of lost primary particles integrated over the azimuthal angle along the collimator surface as a function of the energy deviation. Collimator CE2. Collimator location scheme 2.

4   Scattering and Imperfections

The collimator system of the TTF2 linac is designed to remove particles which can hit the undulators, and for an estimation of the collimation quality we will use the value of a **loss factor** defined as a ratio of the energy deposited in the undulators to the total beam energy. The estimation of the collimation efficiency must include effects of the interaction of collimators and other apertures with the particles themselves (scattering and production of secondaries) and (or) imperfections of the beam optics, because for an ideal beam line and with "black absorbers" as collimators the loss factor is equal to zero.

The purpose of this section is to produce first rough estimations of the loss factor, which will help us to choose between two collimator location schemes and to select collimator material. The more detailed study of scattering and imperfection effects, which we believe can not be separated from a study of imperfections and procedures of theirs correction for the whole TTF2 linac, is better to take as a subject for separate investigations.

4.1   Halo Particles

The accurate estimation of the collimation quality requires the knowledge of the amount of halo particles and their phase space distribution at the entrance of the collimator section, and these objects are not those which can easily be obtained before beginning of the actual operation of the accelerator. The large number of different effects, which could contribute to the halo formation, will turn any attempt of numerical halo simulations into a large time scale project, and it is far beyond our simple desires to get a first feeling about the order of magnitude of the loss factor, and to be able to make a rough comparison of different collimator materials and of the two collimator location schemes.

So, in this section we simply assume that the halo particles account for 1% of the total beam energy, and divide (very loosely) background particles into two categories: the beam halo, which consist of the particles surrounding the beam core; and the distant background, which unites all remaining particles.

As a model of the beam halo, which will be used for the tracking studies in this section, we will use the distribution described below.

34

- Distributions of halo particles in both transverse planes are Gaussian, have $\sigma_{halo}^{x,y} \approx 25 \times \sigma_{beam}^{x,y}$, are matched to the Courant-Snyder ellipses on the entrance of the collimator section, and are finally truncated by the acceptance of the vacuum chamber.

- The energy distribution is also taken Gaussian with $(\Delta E/E_0)_{rms} = 5\%$, and is truncated at an energy deviation of $\pm 12.5\%$ from the nominal beam energy.

- The total number of generated halo particles is taken to be 10^6.

4.2 Effect of Secondary and Scattered Particles

In this subsection we will consider the effect of the interaction of particles with the collimator materials and will neglect effects of their interaction with other apertures and imperfections in the beam optics.

4.2.1 Tracking Procedure for Collimator System Simulations

For the estimation of the loss factor we have used a combination of the TrackFMN particle tracking program [3] and the EGS4 (Electron-Gamma-Shower) Monte-Carlo code [4], so that, between collimators and through undulators particles (electrons, positrons and photons) were transported using TrackFMN, and the passage of particles through tapered collimators was simulated with EGS4. Thus, in our tracking procedure, an impacting particle was able to produce secondary particles or to be scattered only interacting with collimator material. All other beam line apertures were acting as black absorbers, that means that the particle impact energy was recorded in these places as deposited energy.

Figure 20 shows an example of such simulations: ten $1\,GeV$ electrons hit the copper collimator with two essentially different values of impact parameter. One sees the scattered electrons, the secondary particles (green, blue and red trajectories correspond to electrons, positrons and photons, respectively), and the development of the electromagnetic shower inside the collimator material.
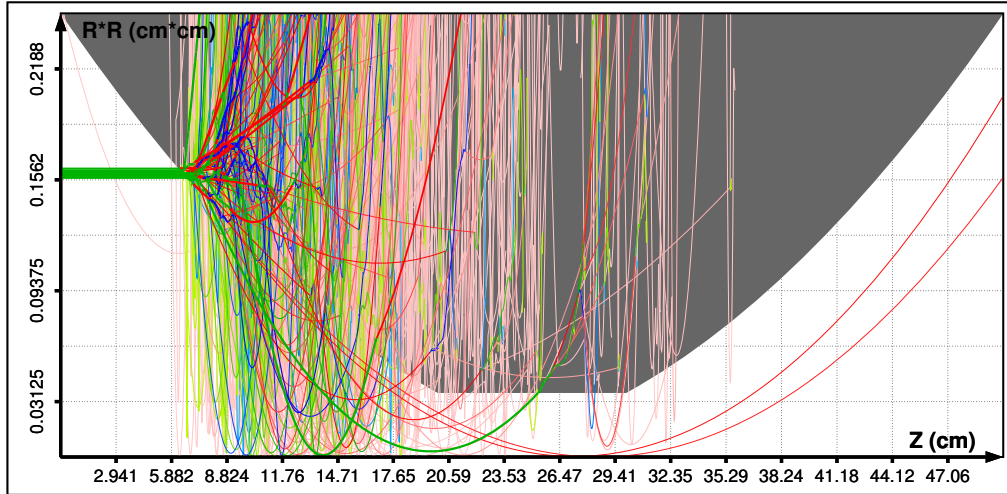
Figure 20: Scattering, production of secondary particles, and development of the electromagnetic shower in the collimator made from copper.

36

4.2.2 Tracking Studies with Gaussian Beam Halo Model

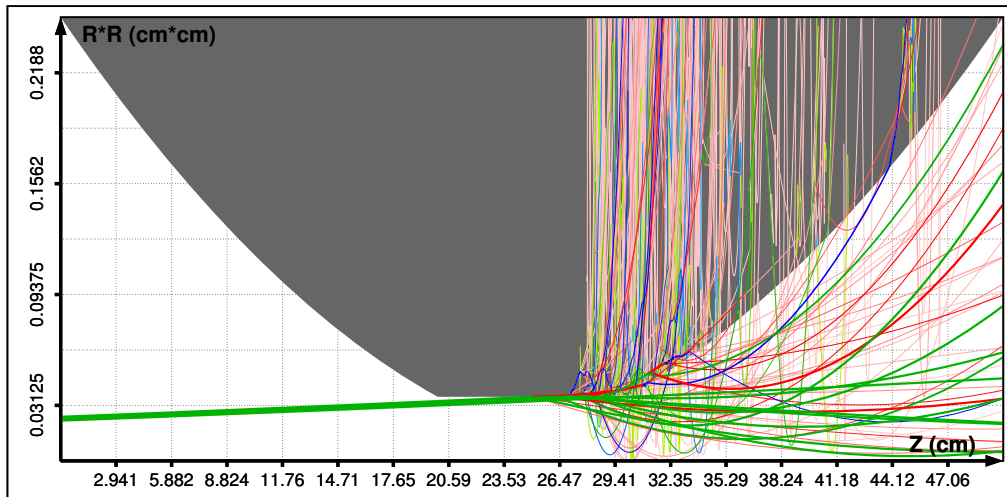Here we summarize the results of our tracking studies with the Gaussian beam halo model obtained for a beam energy of $1\,GeV$ and for the case of copper collimators (titanium collimators will be discussed a little bit later).

Collimator location scheme 1:

- About 2% of particles successfully passed through both, collimator section and undulators, without touching their apertures. The phase space occupied by this particles gives us an idea about the collimator system acceptance and its projections on different coordinate planes can be seen as dark spots in figures 21 and 22.

- The loss factor is defined mainly by the collimator CT2 (last collimator for the scheme 1), since photons produced in the first 3 collimators were not able to reach the undulators at all, and most of the secondary electrons and positrons coming from the first 3 collimators were picked up by the downstream collimators or were lost in the beam pipe.

- 40% of the energy deposited in the undulators was carried by photons (all produced in the collimator CT2), 3% - by positrons, and 57% - by electrons.

- The loss factor was estimated as $\sim 4 \cdot 10^{-6}$.

Figures 21 and 22 show the phase space portraits of primary and secondary electrons on the exit of the CT2 collimator and on the entrance of the undulator section, respectively. One sees that the transmission through the about $3\,m$ long beam line between the exit of CT2 collimator and the entrance of the undulator section reduces essentially the population of secondaries which are outside the collimator system acceptance (seen as dark spots in the cited figures), but a significant amount of secondaries survives and most of them will be lost in the undulator section.

Collimator location scheme 2:

- The percentage of particles, which passed through the collimator section and undulators without touching their apertures, was only about

Figure 21: Phase space portraits of primary and secondary electrons on the exit of the CT2 collimator. Collimator location scheme 1.

38

Figure 22: Phase space portraits of primary and secondary electrons on the entrance of the undulator section. Collimator location scheme 1.

0.5%. It means that for the scheme 2 the acceptance of the collimator system is smaller than for the scheme 1, and it is not surprising, because the collimator apertures for the scheme 2 are tighter.

- The loss factor is completely determined by scattered and secondary electrons and positrons, because the photons produced by collimators were not able to reach the undulator entrance at all (after the last collimator of the scheme 2, CE2, we still have the dipole magnet).

- The loss factor was estimated as $\sim 3 \cdot 10^{-7}$.

Figures 23 and 24 show, for example, the energy distribution of positrons and photons produced by collimator CT1 (first collimator for the scheme 2). Most of the positrons have low energies and they will be lost in the beam line even before reaching the downstream collimator.

Figures 25 and 26 show the phase space portraits of primary and secondary electrons at the exit of the CE2 collimator (last collimator for the scheme 2) and at the entrance of the undulator section. One can see that the transmission through the beam line, which for the scheme 2 is about $10\,m$ long and contains a dipole magnet, reduces the population of secondaries essentially better than in the scheme 1 (compare with figures 21 and 22).

Figure 27 presents the distribution of electron losses in the section downstream of the last collimator and in the undulator section. One sees that low energy secondaries are lost in the beginning of the beam line where the dipole magnet is located.

4.2.3 Distant Background, Non-Gaussian Beam Halo and Pencil Beam Investigations

The simulations presented above were very time consuming due to the huge amount of secondaries produced by 10^6 primary halo particles generated at the entrance of the collimator system. And though we have obtained a lot of helpful information, the resulting loss factor could be considered as being too optimistic (or, for someone, too pessimistic). What is possible to do and how can we get some feeling about the dependence of the loss factor on the initial particle distribution without repeating such calculations for a large variety of beam halo models? We decided to make pencil beam investigations, searching for the worst possible collimator impact scenario, the scenario which will result in the largest energy deposited in the undulators.
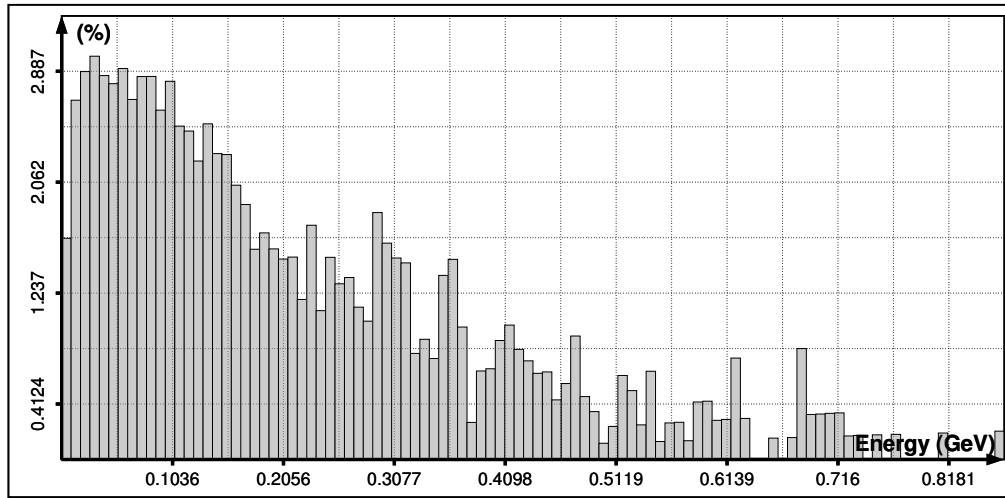
Figure 23: Distribution of positron energies at the exit of the CT1 collimator. Collimator location scheme 2.
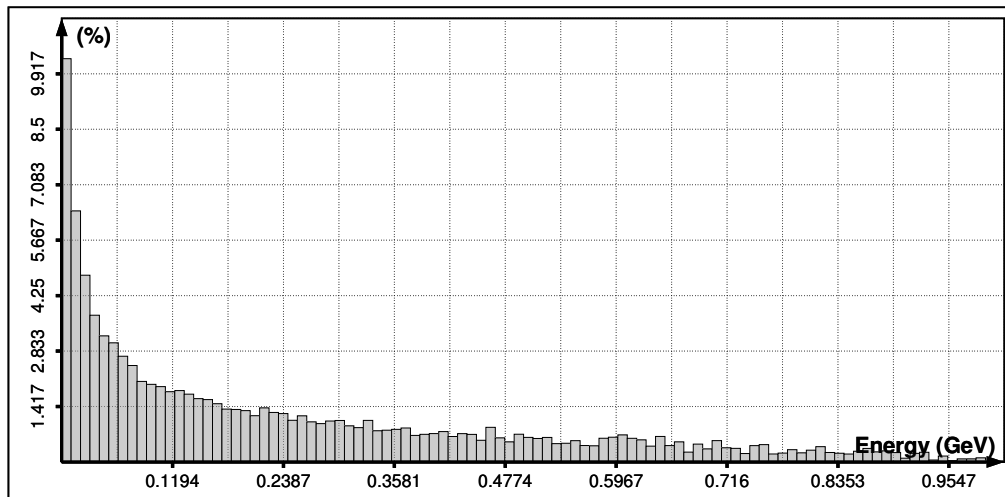
Figure 24: Distribution of photon energies at the exit of the CT1 collimator. Collimator location scheme 2.
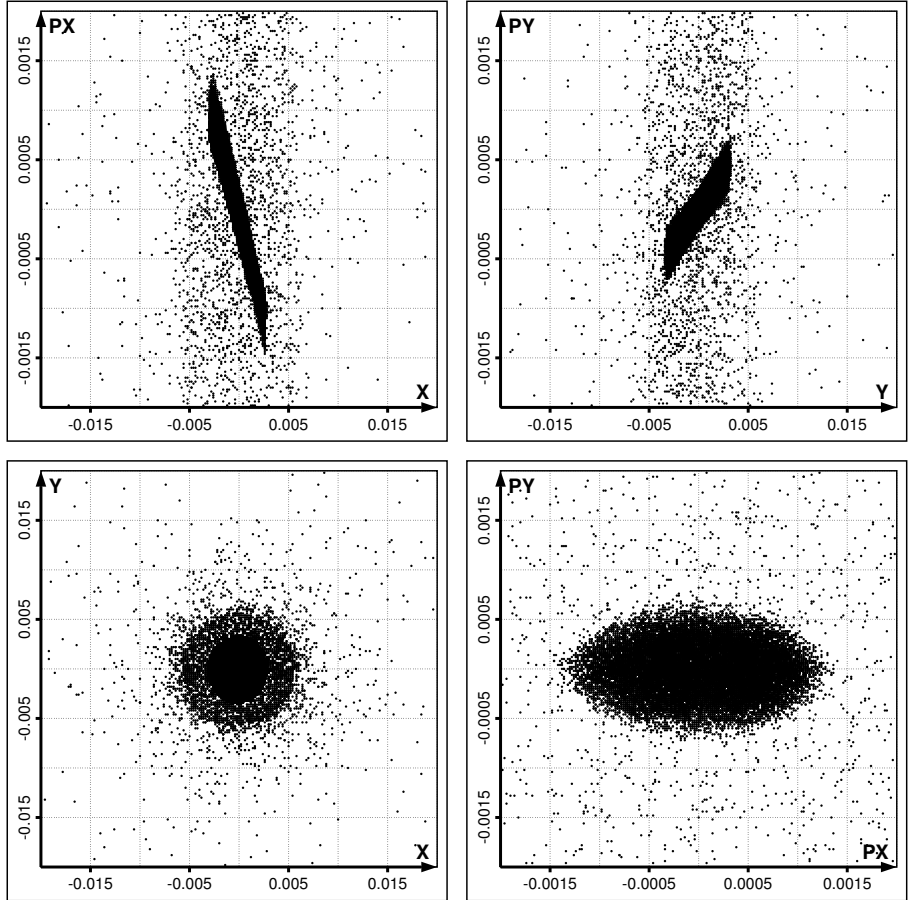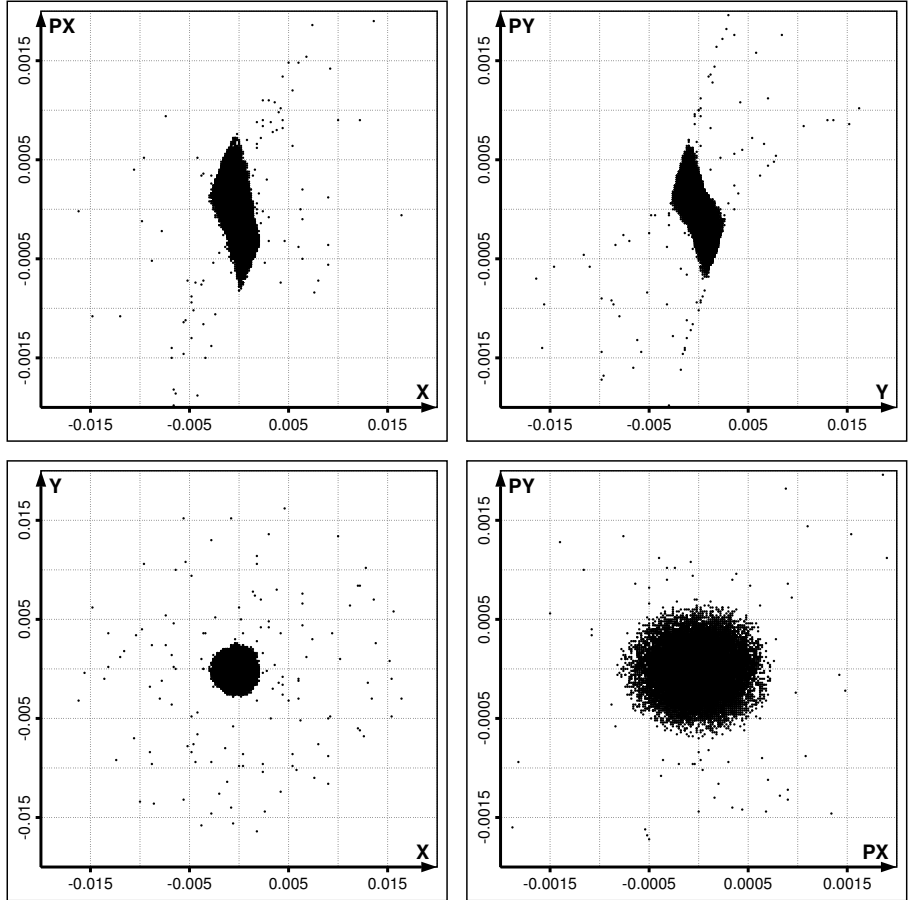
41
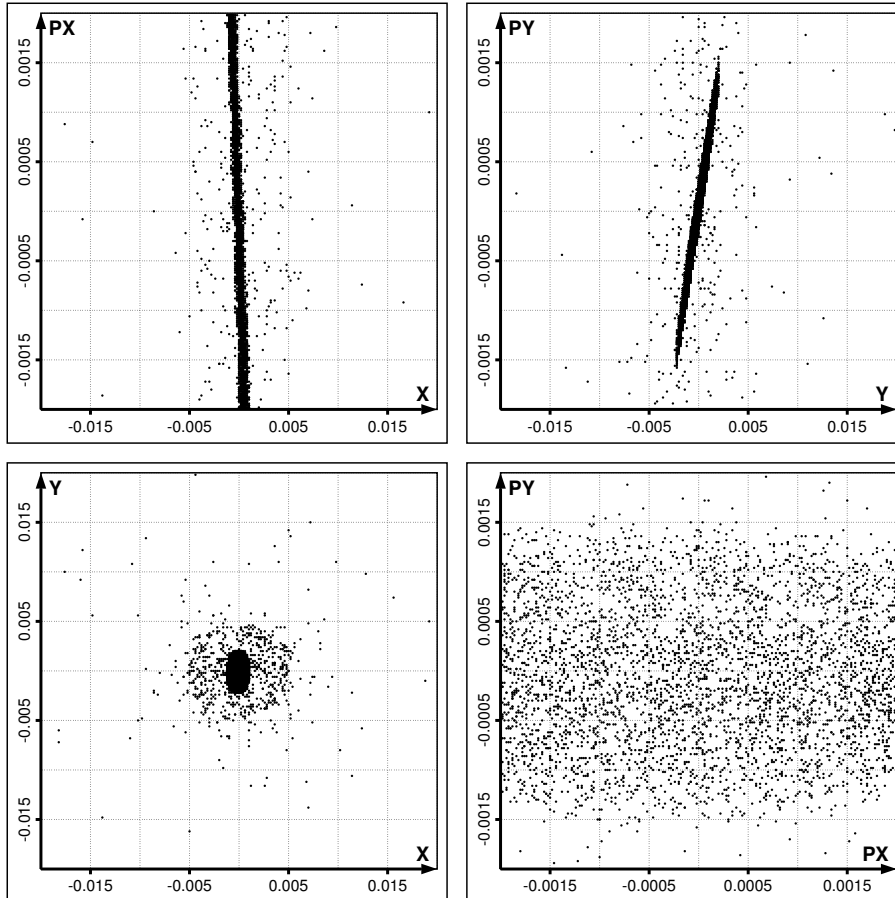
Figure 25: Phase space portraits of primary and secondary electrons at the exit of the CE2 collimator. Collimator location scheme 2.
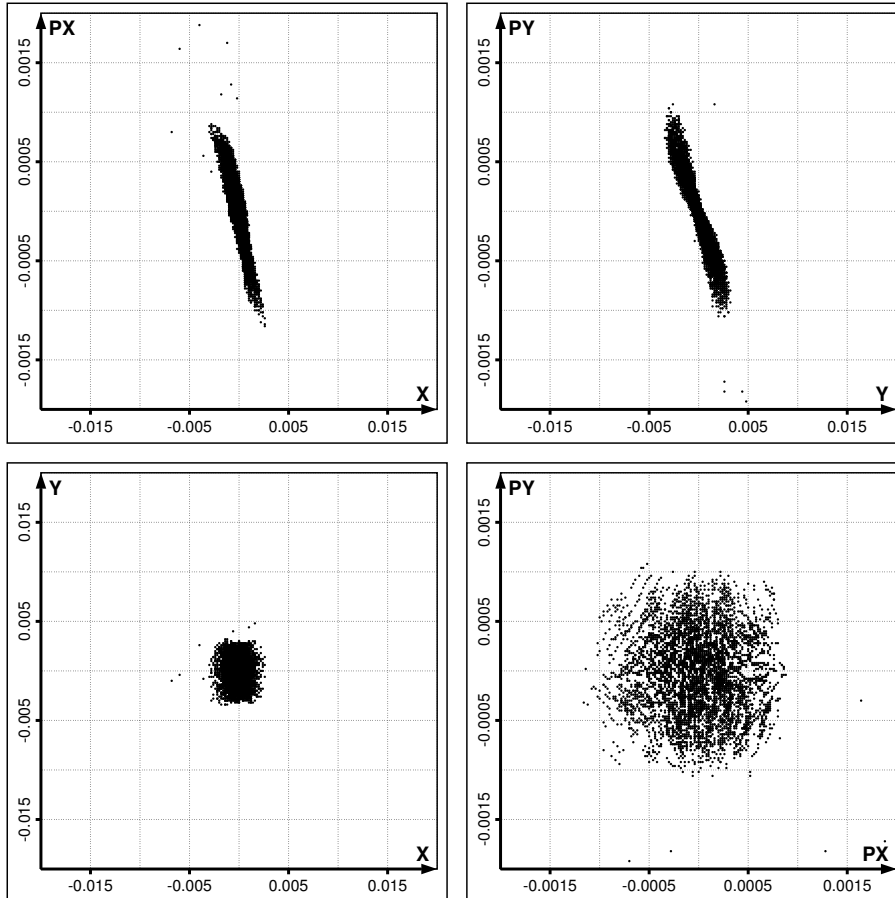
Figure 26: Phase space portraits of primary and secondary electrons at the entrance of the undulator section. Collimator location scheme 2.
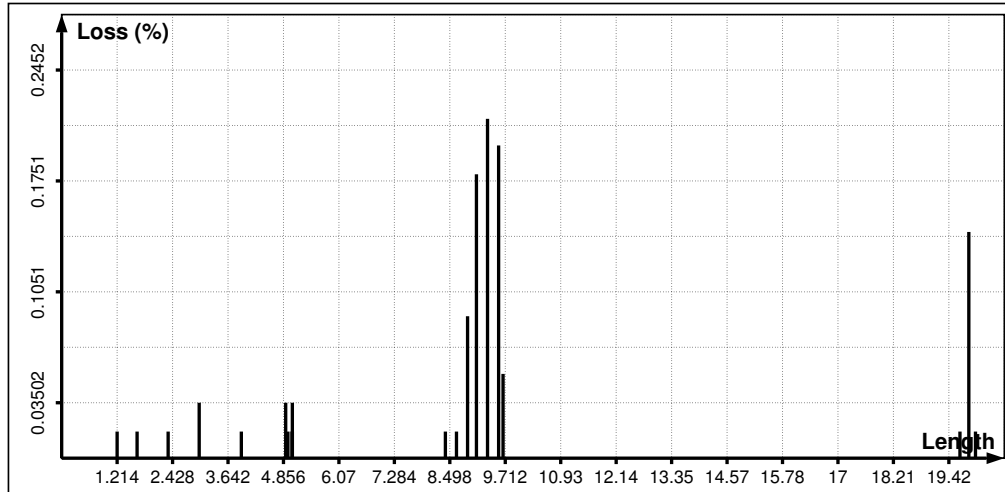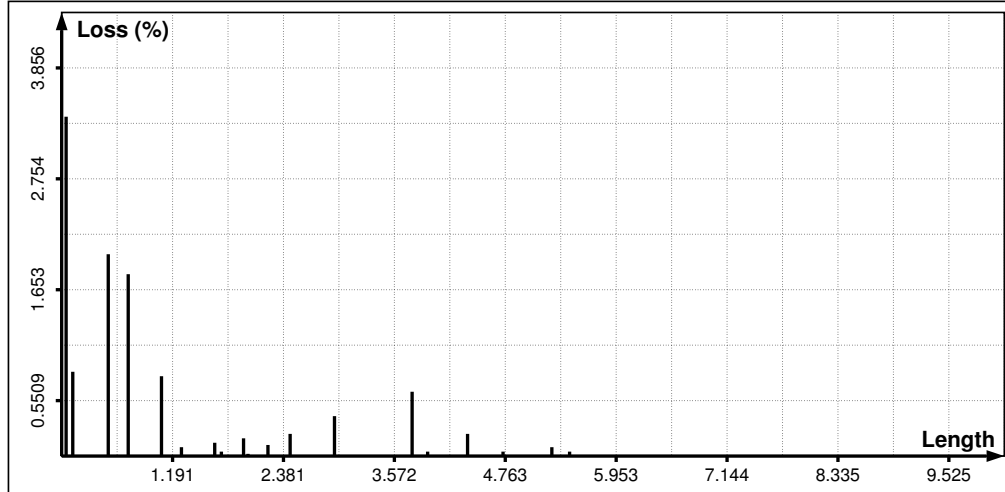
Figure 27: Electron losses along the beam line between the exit of the collimator CE2 and the entrance of the undulator section (top), and along the undulator section (bottom). Collimator location scheme 2.
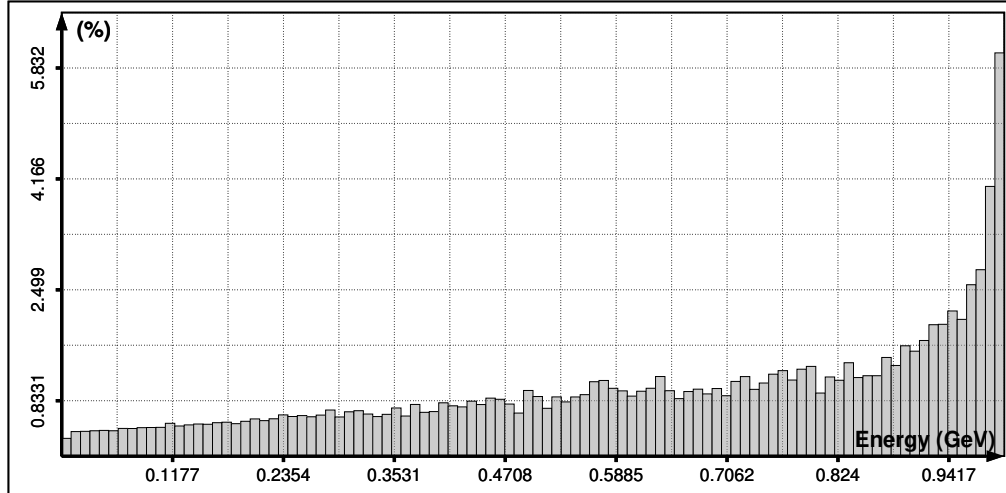
Figure 28: Distribution of scattered and secondary electron energies at the exit of a copper collimator after its main part was hitted by a pencil beam with small impacts angle.

This, worst-case, approach will allow us to make rough an upper estimate of the loss factor even without having in mind a particular beam halo model.

We made an extensive numerical study, during which we hit the collimator surfaces by pencil beams carring $2 \cdot 10^5$ primary $1\,GeV$ electrons and then trace the resulting scattered and secondary particles through the downstream beam line and the undulator section, and record the deposited energy in the undulators. For the distribution of impact positions and angles, we have used results of our advanced tracking studies with primary particles which are partly shown in figures 12 - 19.

Figure 28 shows an example of such calculations, the distribution of scattered and secondary electron energies at the exit of copper collimator after its main part was hitted by the primary pencil beam with impact angle similar to those shown in the lower part of figure 20.

As it could be expected from the beginning, the worst-cases were obtained when the pencil beam was fired into the main part of the last collimator for each scheme (CT2 for scheme 1, and CE2 for scheme 2) or into the section of the entrance taper closest to this part (as close as a fraction of a millimetre) having small impact angle, and the corresponding numbers are summarized

45

below for the case of collimators made from copper.[10]

- **Collimator location scheme 1. Copper collimators.**

  The scattered and secondary particles transmit $\sim 68.3\%$ of the initial pencil beam energy ($\sim 41.6\%$ by electrons, $\sim 2.7\%$ by positrons, and $\sim 24\%$ by photons) through the collimator exit, and more that $\sim 20\%$ of the input energy is recorded to be lost in the undulator.

- **Collimator location scheme 2. Copper collimators.**

  The scattered and secondary particles transmit $\sim 47.8\%$ of the initial pencil beam energy ($\sim 21.1\%$ by electrons, $\sim 2.8\%$ by positrons, and $\sim 23.9\%$ by photons) through the collimator exit, but only $\sim 1\%$ of the input energy is recorded to be lost in the undulator.

Note that the difference in energies transmitted through the collimator exit comes mainly from the difference of radii of their inner collimating tubes.

What kind of conclusions can we make now, without a knowledge of the beam halo distribution, about the value of the loss factor? Let us consider, for example, the collimator location scheme 2.

- If, in the emergency case, the whole mis-steered beam will be able to reach the last collimator and hit its main part with a small impact angle, then the energy deposited in the undulators can be as large as 1% of the total beam energy.

- If, during normal linac operation, halo particles (as we have assumed before, that is about 1% of the total beam energy) will be distributed so exoticly that all of them will be able to reach the last collimator and hit its main part with small impact angles, then the loss factor can approach the value 10^{-4}.

- According our advanced tracking studies with primary particles, less than 1% of particles, which reach the last collimator, are able to hit its main part. So, if we will assume that the distribution of halo particles is

---

[10]For the cases when the pencil beam hit other parts of the last collimator or an arbitrary point of any from the first three collimators, the resulting deposited energy in the undulators will be smaller by orders of magnitude.

not very exotic and has some kind of uniformity in the impact positions, then we may conclude that for routine linac operation the loss factor should not exceed $\sim 10^{-6}$.

Calculations for the case of titanium collimators were done only for scheme 2, because at this point it was already clear that this scheme will be chosen.

- **Collimator location scheme 2. Titanium collimators.**

  The scattered and secondary particles transmit $\sim 74.6\%$ of the initial pencil beam energy ($\sim 37.2\%$ by electrons, $\sim 3.5\%$ by positrons, and $\sim 33.9\%$ by photons) through the collimator exit, and $\sim 1.8\%$ of the input energy is recorded to be lost in the undulator.

One sees that usage of titanium as collimator material could increase the loss factor almost twice in comparison to copper.

4.3 Sensitivity to Errors

Being afraid of possible degradation of the beam quality due to collimator wakefields, we have chosen the collimator apertures to be as large as possible, that is very close to the border of the set of protecting apertures.[11] Thus alignment and field errors of the beam line elements may have a strong effect on the collimation quality, because the chosen apertures may appear to be already outside of the set of protecting apertures, when calculated with imperfections taken into account.

To study that kind of sensitivity to the imperfections, the Gaussian halo described previously was many times tracked through the beam line with randomly generated alignment and field errors and the resulting loss factors were recorded. Errors were generated in groups, several seeds for every fixed rms values, and the rms values, in the next turn, were varied within some interval. In the end, the averaged loss factor for every group of errors was found, and the resulting averaged loss factor will be presented below as a function of the rms values. Note, that imperfections for the undulators and for the quadrupoles between undulators were not considered, the safety factor for the undulator aperture was kept unchanged ($s_f = 0.9$), and scattering

---

[11]The distance to the border was defined by the safety factor ($s_f = 0.9$), used for the undulator aperture.

Table 3: Design manufacturing and installation tolerances of the TTF2 magnets (rms values).

	σ	Units	Symbol
Dipole field error	5×10^{-4}		$\Delta B_0/B_0$
Quadrupole field error	2×10^{-3}		$\Delta B_1/B_1$
Sextupole field error	2×10^{-3}		$\Delta B_2/B_2$
Horizontal displacement	300	μm	Δx
Vertical displacement	300	μm	Δy

and production of secondaries were not included. Alignment and field errors were generated according to a Gaussian distribution truncated at 2 standard deviations.

Collimator location scheme 2 was chosen for the investigation and no correction algorithm was used in the simulations, because we were mainly interested to see the effect of the unavoidable vibration of magnets and fluctuations of their fields on short time scales during linac operation. As a tolerable upper level of the average loss factor we have taken the value 10^{-6}.

Figure 29 shows the averaged loss factor as a function of the rms value of transverse horizontal and vertical displacements of quadrupoles and sextupoles. One sees that the tolerable limit of transverse displacements is about $65\,\mu m$ (rms).

The field errors were studied separately for the different types of magnets. Figure 30 shows the effect of quadrupole and sextupole field errors, and figure 31 presents result obtained for dipole field imperfections. We see that the average loss factor is quite insensitive to the field errors. The tolerable limits are 2% for quadrupole and sextupole, and 1.2% for dipole field errors, respectively. That is much higher than the manufacturing design tolerances of TTF2 magnets manufacturing listed in table 3.

Finally, figure 32 shows the combined effect of alignment and field errors. Field errors were generated (now for magnets of all types) using fixed rms values taken from table 3, and the rms value of transverse displacements was varied. One sees that the presence of the field errors reduces the tolerable limit of transverse displacements quite inessentially, from $65\,\mu m$ to $60\,\mu m$.

So the alignment errors affect the collimation quality more seriously than the field errors, and further detailed studies of correction algorithms and their effect on the collimation is needed.
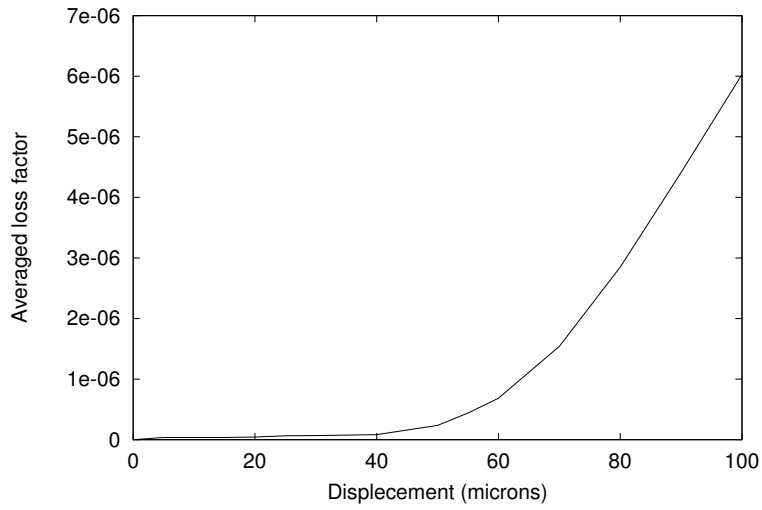
Figure 29: Averaged loss factor as a function of the rms value of transverse horizontal and vertical displacements of quadrupoles and sextupoles.

Figure 30: Averaged loss factor as a function of the rms value of quadrupole and sextupole field errors.

Figure 31: Averaged loss factor as a function of the rms value of dipole field errors.

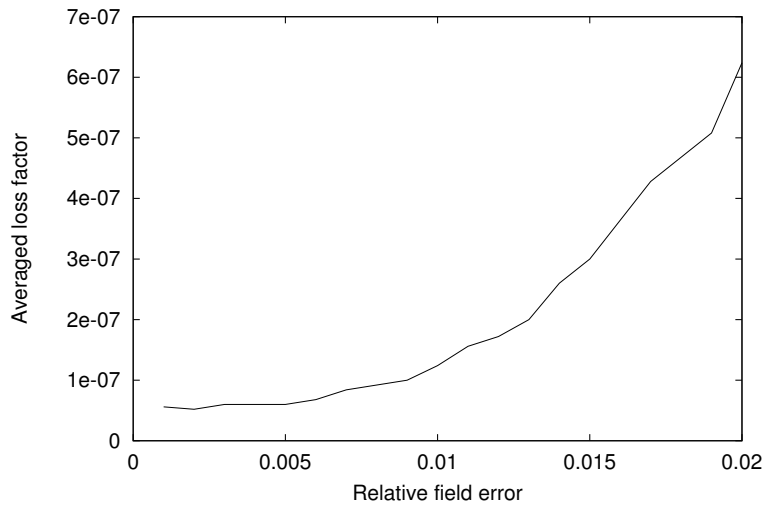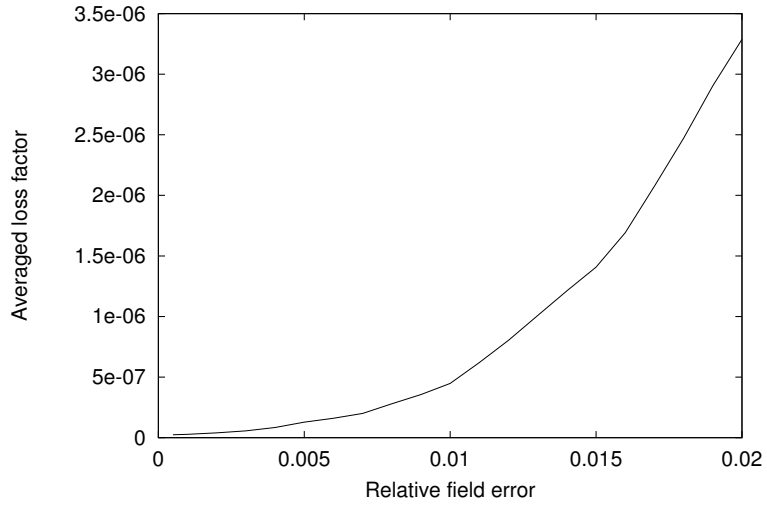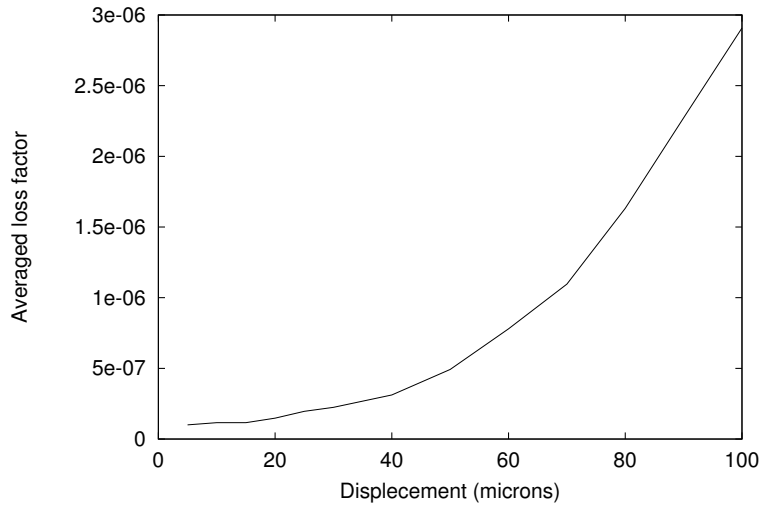Figure 32: Averaged loss factor due to alignment and field errors together as a function of the rms value of transverse displacement of quadrupoles and sextupoles.

50

5 The Heat Load on Collimators Under Normal Operating Conditions

Under normal operating conditions the heat load on the collimators should be relatively low compared to the total beam power. Often $1\% - 2\%$ losses are assumed. With the achievement of the design parameters the average beam power of the TTF2 linac will be about $72\,kW$, and that will give us the loss value of $(720 - 1440)\,W$.

When this study was done the exact mechanical design of the collimators was not yet known, and because the distribution of impacting particles is anyway hardly predictable, we will consider a simplified 1D axisymmetric heat conduction problem with uniform heat load along length and azimuthal angle, but with the over-estimating assumption that 2% of the average beam power is absorbed by the inner surface of a single collimator of a reduced length of $10\,cm$ (that means that $10\,cm$ of the collimator have to be capable of continuously absorbing $\bar{P}_{av} = 1440\,W$).

5.1 1D Axisymmetric Radial Heat Conduction

Consider an infinitely long cylindrical collimator with uniform heat conductivity, which has an inner radius r_0 and an outer radius r_f. If the density of internal heat sources Q_r does not depend on the azimuthal angle and longitudinal position, then this problem involves only a single dimension of heat conduction, and the distribution of temperature in the collimator can be obtained as solution of the heat conduction equation

$$\rho\, c_p\, \frac{\partial T}{\partial t} \;=\; k\, \frac{1}{r}\frac{\partial}{r}\left(r\, \frac{\partial T}{\partial r}\right) \;+\; Q_r(r,\,t)\,, \tag{2}$$

where r describes the radial position normal to the axis of symmetry, ρ is the density of the material, c_p is the specific heat, and k is the heat conductivity[12].

To specify the unique solution we need to add to the problem boundary and initial conditions and have to determine the function $Q_r(r,\,t)$.

---

[12]We consider not a cylindrical block of the length $l = 10\,cm$, but an infinitely long collimator. It gives no difference, if we assume that the block edges are insulated (no passage of heat through them).

5.1.1 Initial Condition

As the initial state we shall assume that the collimator has room temperature

$$T(r, 0) = T_{room} \, .$$

5.1.2 The Boundary Conditions on the Inner Surface

Energy can be released from the inner collimator surface in form of photons (electromagnetic waves). The total energy flux q emitted per unit area and time into vacuum is given by

$$q = \varepsilon \, \sigma \, T^4 \, , \tag{3}$$

where σ is the Stefan-Boltzman constant and ε is the emissivity of the surface.

$$\sigma = 5.67 \times 10^{-8} \; \left(W \cdot m^{-2} \cdot K^{-4} \right) \, . \tag{4}$$

The radiant energy will be partly absorbed back into the collimator after multiple reflections (metals have low absorptivity and high reflectivity values), and partly will be transmitted out through the collimator hole. So even if we shall neglect the absorbed energy, heat transfer by thermal radiation leads to the non-linear boundary condition

$$k \cdot \left. \frac{\partial T}{\partial r} \right|_{r=r_0} = \left. \varepsilon \, \sigma \, T^4 \right|_{r=r_0} \tag{5}$$

which complicates the problem. Taking into account that, for example, in the case of the copper collimator of $0.5 \, m$ length and with inner radius of $0.002 \, m$ the amount of heat which can be transferred by thermal radiation is approximately $5 \, W$ at temperature $100°C$ and $3 \, W$ at $50°C$, we shall neglect this effect, and shall consider the inner collimator surface as insulated (no passage of heat through it):

$$\left. \frac{\partial T}{\partial r} \right|_{r=r_0} = 0 \, . \tag{6}$$

5.1.3 The Boundary Conditions on the Outer Surface

We shall assume that the outer collimator surface is cooled by circulating water. Using Newton's law of the heat exchange between a surface at a temperature T and water in contact with it at the characteristic temperature T_w we obtain

$$-k \cdot \frac{\partial T}{\partial r}\bigg|_{r=r_f} = h \cdot (T|_{r=r_f} - T_w), \tag{7}$$

where h is the convection heat transfer coefficient, and $\lambda = h/k$ is the coefficient of heat exchange.

In general, the heat transfer coefficient can be obtained by a solution of the Navier-Stokes equations describing the flow of a viscous fluid and the related energy equation, or it can be found experimentally. For the present study we have taken some approximate empirical formulae which are generally used with good results (see, for example, [5], [6], and [7]) and which gives us the value of $h \approx 0.4$ $(W \cdot cm^{-2} \cdot K^{-1})$. Though we do not know yet the exact value of the contact area between the water and the collimator material, we used some reduced values for h in the range $0.05 - 0.3$.

5.1.4 The Density of Internal Heat Sources

The density of internal heat sources integrated over the collimating block volume and then averaged over a characteristic time interval t_c must give us the average power absorbed by the collimator

$$\frac{1}{t_c} \int_{t_c} \int_0^l \int_0^{2\pi} \int_{r_0}^{\infty} r \, Q_r(r,\, t) \, dz \, dr \, d\phi \, dt = \bar{P}_{av}. \tag{8}$$

Note that the integration over the radius is made in (8) not from r_0 to r_f, but from r_0 to infinity. This means that we consider $\bar{P}_{av}$ not as the actual absorbed power, but as the power which could be absorbed in the limit of an infinitely thick collimator.

And though we have already assumed that Q_r does not depend on the azimuthal angle and longitudinal position, we will make an additional simplification and will consider this function in the form

$$Q_r(r,\, t) = H \cdot r_0 \cdot q_t(t) \cdot q_r(r), \tag{9}$$

53

where the nonnegative functions $q_t(t)$ and $q_r(r)$ satisfy

$$\int_{r_0}^{\infty} \tau q_r(\tau)\, d\tau \;=\; 1 \quad \text{and} \quad \frac{1}{t_c} \int_{t_c} q_t(\tau)\, d\tau \;=\; 1\,. \tag{10}$$

Here the constant H, according to (8), is equal to $\bar{P}_{av} / (2\pi r_0 l)$ and has the meaning of power absorbed per unit surface area of the inner collimating tube.

The function $q_t(t)$ describes the time structure of the heat load on the collimator and will be specified later on, separately for stationary and non-stationary cases.

It seems to be the natural choice for the radial distribution function $q_r(r)$ to make it directly proportional to the energy density deposited per unit longitudinal length in the collimator material. So we face the problem to determine the energy deposition density, which, in the next turn, in order to be well defined forces us to make assumptions about the distribution and energies of the impacting particles. The number of choices is pretty large and what actually was used for the calculations presented in this section can be shortly summarized as follows.

- The energy deposition density was obtained from a shower simulation using the EGS4 program. As material geometry we have used a one meter long cylinder with inner radius $2\,mm$ and, in order to avoid an essential number of particles to escape transversely, large outer radius of $20\,cm$.

- The impacting electrons were distributed uniformly along the cylinder length and their initial velocities were chosen to be in a single (longitudinally axis-centered) plane. The incident angle and energy were chosen to be the same for all electrons, $2°$ and $1\,GeV$, respectively.[13]

- The energy deposition density obtained was initially integrated over the azimuthal angle, then averaged over the cylinder length, and after that normalized in accordance with (10). Final results for copper and titanium can be seen in figure 33.

---

[13] $2°$ is the average angle at which primary particles can hit the inner surface of the collimators (their tapers and main parts), the maximal angle being of about $5°$. This information was obtained during tracking studies with primary particles, which were already partly described in the above sections.
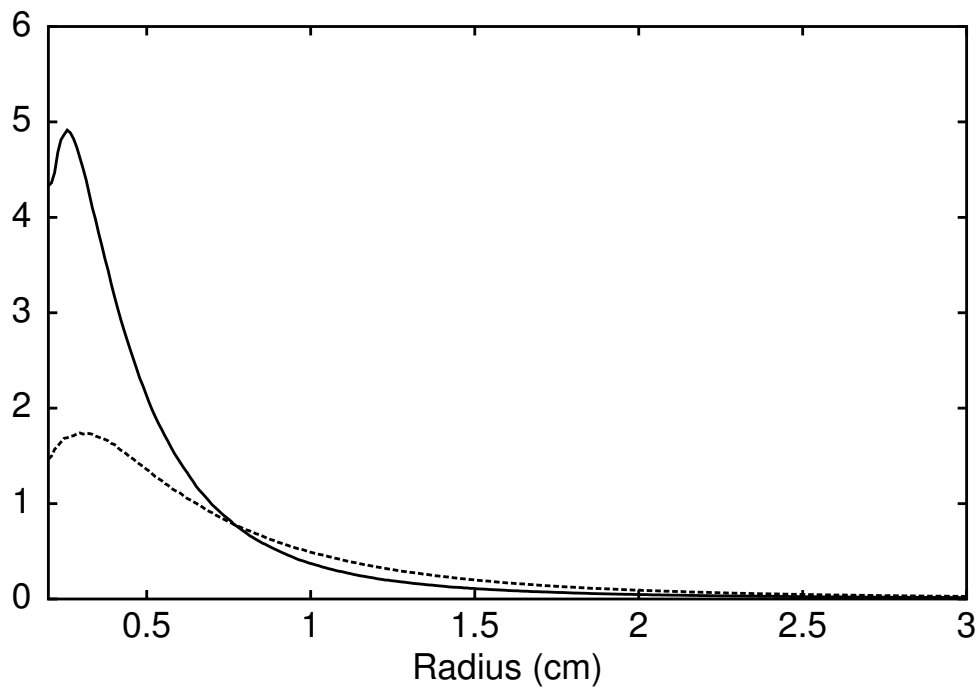
Figure 33: The function $q_r(r)$ for titanium (dotted line) and for copper (solid line).

5.1.5 Solution of Stationary Problem

The stationary solution of equation (2) with the function $q_t(t) \equiv 1$ (uniform heat load in time), and with the boundary conditions (6) and (7) is simply given by the following formula

$$
T(r) \; = \; T_w \; + \; \frac{r_0}{r_f} \frac{H}{h} \int\limits_{r_0}^{r_f} \tau q_r(\tau)\, d\tau \; + \; r_0 \frac{H}{k} \int\limits_{r}^{r_f} \frac{1}{\tau} \left(\int\limits_{r_0}^{\tau} \xi q_r(\xi) d\xi \right) d\tau . \quad (11)
$$

From (11) it can be seen that the temperature decreases monotonically with radius and therefore the maximum value T_{max} is always reached at $r = r_0$ ($T_{max} = T(r_0)$).

5.1.6 Optimal Distance for Water Cooling Placement

Formula (11) is very well known and can be found in most textbooks dealing with heat conduction problems, and, nevertheless, it contains one interesting property which, it seems to be, never was noticed before. Let us examine the maximum temperature T_{max} as the function of r_f. Calculating the derivative

$$
\frac{\partial T_{max}}{\partial r_f} \; = \; \frac{r_0}{r_f} \frac{H}{h} \left(r_f q_r(r_f) \; + \; \left(\lambda - \frac{1}{r_f} \right) \int\limits_{r_0}^{r_f} \tau q_r(\tau)\, d\tau \right) \qquad (12)
$$

we see that for the case when $r_f > \lambda^{-1}$ this derivative is positive and hence the maximum temperature simply increases with further increasing of r_f. But in the region $r_f \leq \lambda^{-1}$ the inner surface temperature may reach a minimum for a certain value of r_f, which thus will define the optimal distance for water cooling placement. A sufficient condition for the existence of such a minimum, which we will call the **heat localization condition**, is that $r_0 < \lambda^{-1}$ and the density of internal heat sources is localized in the region $r_0 \leq r < \lambda^{-1}$ (i.e. function $q_r(r)$ equal to zero or small enough for $r \geq \lambda^{-1}$). In this case T_{max} reaches a minimum for $r_f \approx \lambda^{-1}$ and then will go to infinity logarithmically as $r_f \to \infty$.

$$
T_{max} \; = \; const \; + \; r_0 \cdot H \cdot \left(\frac{1}{h\, r_f} \; + \; \frac{1}{k} \, \ln(r_f) \right) \qquad \text{for} \quad r_f > \lambda^{-1}.
$$

Figure 34: Difference $T_{max} - T_w$ ($°C$) as a function of outer water cooled radius r_f for $h = 0.01, 0.02, 0.03, 0.05, 0.1, 0.3$ (upper to lower curves).

It is important to note, that if the heat localization condition is satisfied, then the resulting optimal distance for water cooling placement does not depend on H and is insensitive to the details of the profile of the function $q_r(r)$.

Figures 34 and 35 show us, for titanium and copper, the difference $T_{max} - T_w$ as a function of the outer, water cooled radius r_f for several different values of the convection heat transfer coefficient h. One sees in the case of titanium (figure 34), that the optimal distance for water cooling placement exists for $h \leq 0.03$, but under our assumption about the absorbed power it results in temperatures T_{max} which are well above the water boiling temperature, and thus this existence of an optimal cooling distance does not have a practical meaning. In the case of copper the situation changes. Figure 35 shows that for $h \leq 0.5$ it is even better to move the water cooled boundary away from the heat source that can not only decrease the maximum stationary temperature, but is also more safe from the point of
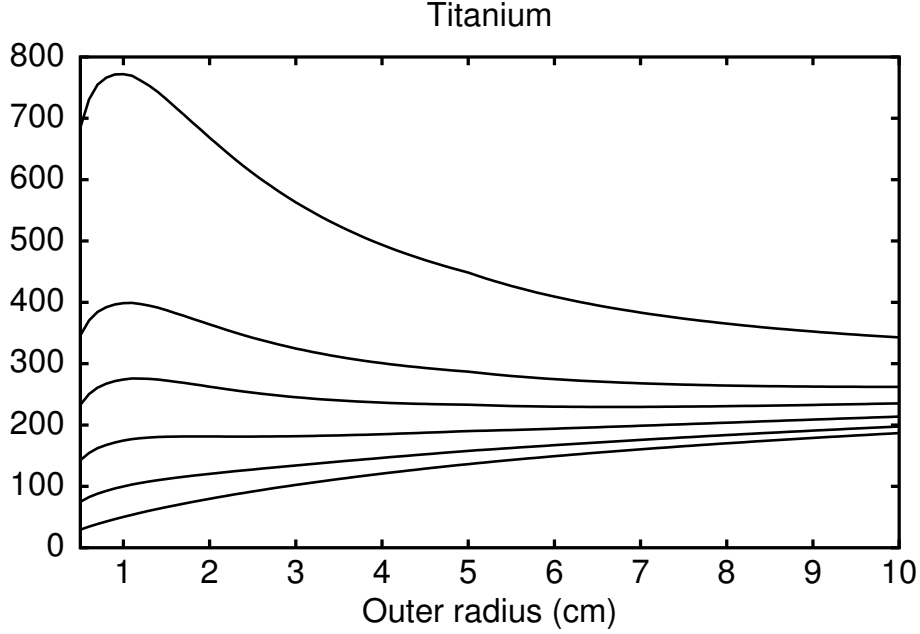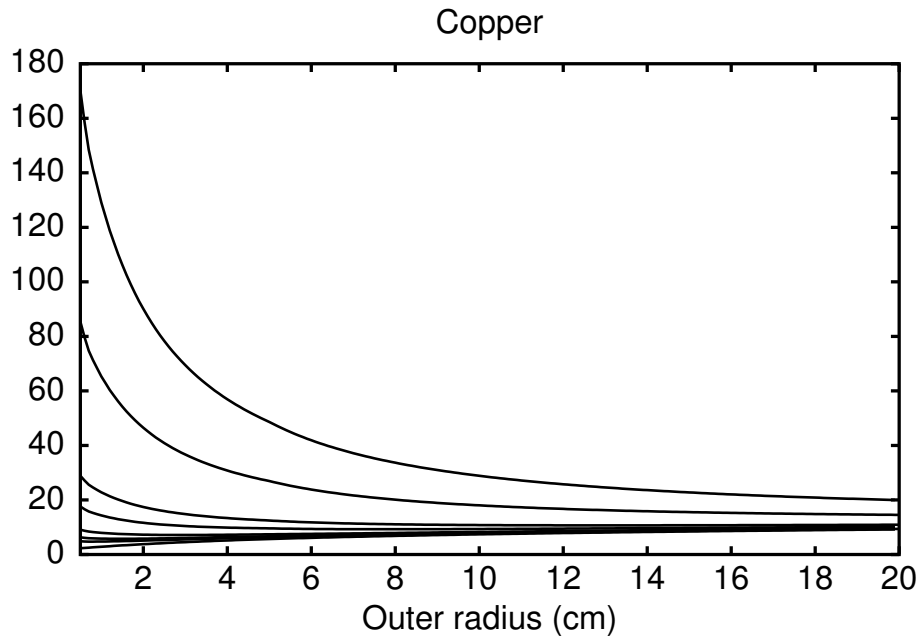
Figure 35: Difference $T_{max} - T_w$ ($°C$) as a function of outer water cooled radius r_f for $h = 0.05, 0.1, 0.3, 0.5, 1.0, 1.5, 2.0, 3.0$ (upper to lower curves).

view of minimization of direct deposited power in the water.[14]

It is interesting to note that the possibility for the existence of the optimal distance for the water cooling placement does not take place for the case of a flat (that is effectively one-dimensional) problem geometry. To illustrate that, let us consider a semi-infinite slab of material of thickness z_f, which is uniformly bombarded from one side by electrons and is cooled from the other side by water. The stationary solution of this problem is given by the formulae

$$T(z) \; = \; T_w \; + \; \frac{H}{h} \int\limits_0^{z_f} q_z(\tau)\, d\tau \; + \; \frac{H}{k} \int\limits_z^{z_f} \left(\int\limits_0^{\tau} q_z(\xi)d\xi \right) d\tau \qquad (13)$$

and obeys the following set of equations and boundary conditions

$$k\,\frac{\partial^2 T}{\partial z^2} \; + \; H \cdot q_z(z) \; = \; 0\,, \qquad \int\limits_0^{\infty} q_z(\tau)\, d\tau \; = \; 1\,, \qquad (14)$$

$$\left. \frac{\partial T}{\partial z} \right|_{z=0} \; = \; 0\,, \qquad -k \cdot \left. \frac{\partial T}{\partial z} \right|_{z=z_f} \; = \; h \cdot \left(T|_{z=z_f} \; - \; T_w \right). \qquad (15)$$

It is easy to check, that $T_{max} \; = \; T(0)$ always increases with increasing of z_f, and thus no optimal cooling distance is available.

Similary, one may analyse the spherical geometry and see that the heat localization condition becomes less bounding than in the cylindrical case.

5.1.7 Nonstationary Problem and Steady-State Regime

For the numerical solution of the nonstationary problem we have used the Crank-Nicholson finite-difference scheme combined with the chasing method [8].

The solution of the nonstationary problem gives us the estimation of the transition time from initial room temperature to steady-state oscillations,

---

[14]To achieve $h > 0.5$ in practice is already not the easiest problem. Especially if one will take into account that cooling water is usually moved through a limited number of pipes and is not in full contact with the outer collimator surface. So, for copper, the existence of an optimal distance for the water cooling placement is of practical importance for our investigations.

and further periodic thermal cycling of the steady-state solution in the neighbourhood of the solution of the stationary problem. The time structure of the heat load on the collimator was chosen to be periodic

$$q_t(t + \tau_p) \equiv q_t(t), \tag{16}$$

where for one period we have (with t_c in (8) equal τ_p)

$$q_t(t) = \begin{cases} \frac{\epsilon}{\tau_t} & \text{if} \quad 0 < t \leq \tau_t, \\[2mm] \frac{\tau_p - \epsilon}{\tau_p - \tau_t} & \text{if} \quad \tau_t < t \leq \tau_p. \end{cases} \tag{17}$$

Here τ_t is the time of the train passage and $\tau_p - \tau_t$ gives the time interval between two trains.

Parameter ϵ ($0 \leq \epsilon \leq \tau_p$) describes the relative time distribution of the collimator heating. For $\epsilon = \tau_t$ we have a uniform heat load in time (like in the case of the above considered stationary problem). If $\epsilon = \tau_p$, then the energy is absorbed by the collimator only during the train passage. The different values of ϵ were considered by numerical calculations with the result that the maximum values of the steady state relative oscillations of the temperature are achieved when the value of ϵ approaches τ_p.

According to (17) the function $q_t(t)$ has a constant value during the passage of the train of bunches, and another, again constant, value in the time interval which separates two trains. The further structuring of the heat load on the collimators in time (assuming, for example, that the heat load on the collimators has local maximums accompanying individual bunches inside a train) does not increase the relative temperature oscillations because already on the train passage time scale τ_t the heating can be considered as instantaneous.

5.1.8 Results for Titanium

It was already pointed out above, that in the case of titanium for having reasonable stationary temperatures without decreasing the heat load assumptions, one needs to move the cooling water close to the inner collimator surface and to provide a large enough value of the heat transfer coefficient.

Assuming that $T_{room} = T_w = 25°C$ and the heat transfer coefficient $h = 0.1$, we obtain that $T_{max} = 112°C$ for $r_f = 0.5\,cm$ and $T_{max} = 128°C$ for $r_f = 1\,cm$. For $h = 0.3$ this temperatures are $64°$ and $82°$,

respectively. Note that these values of r_f already give us problems with the power directly deposited in the cooling water by the shower particles and, consequently, with water activation.

The periodic thermal cycling of the titanium temperature subjected to successive $\tau_t = 800\,\mu s$ pulses every $\tau_p = 0.1\,s$ is shown in figure 36 for $r_f = 1\,cm$ and $h = 0.3$. The lower part of the figure displays the same history for the first 10 pulses. The blue line corresponds to the case $\epsilon = \tau_t$ (uniform heat load in time), and the red line corresponds to the case $\epsilon = \tau_p$ (heating only during the train passage).

5.1.9 Results for Copper

We have already discussed the practical consequences of the existence of the optimal distance for the water cooling placement in the case of a copper collimator. And here, just for comparison, we show in figure 37 the nonstationary temperature evolution for the same values of h and r_f as for titanium. The steady state temperature is reached after approximately 150 pulses, when the energy gained by heating is equal to energy lost by cooling. For the considered parameters the maximum temperature is around $50°C$. The relative temperature oscillations are about $5°C$.
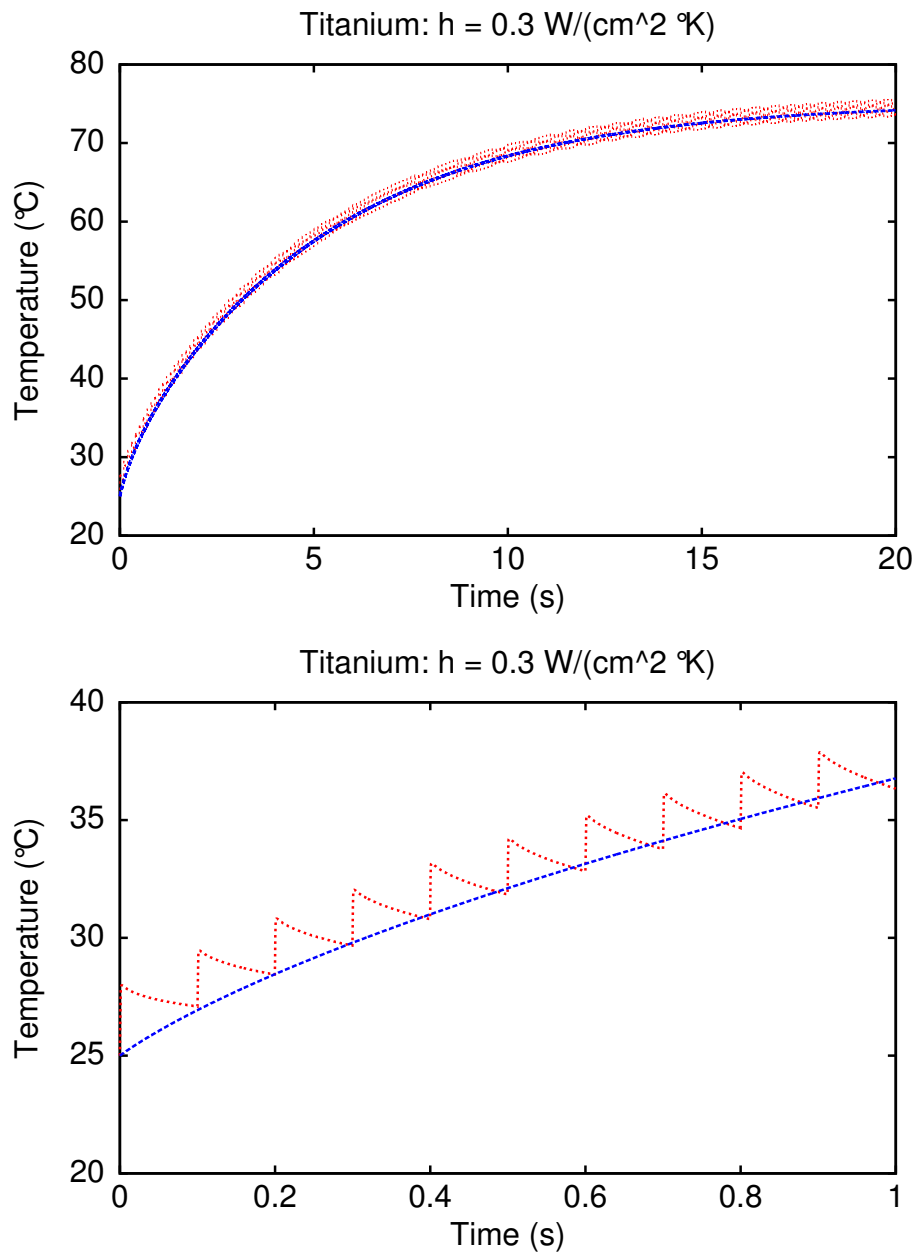
Figure 36: Transition of inner surface temperature from initial room temperature to steady-state oscillations for a titanium collimator. The lower figure is an enlarged part of the upper figure.
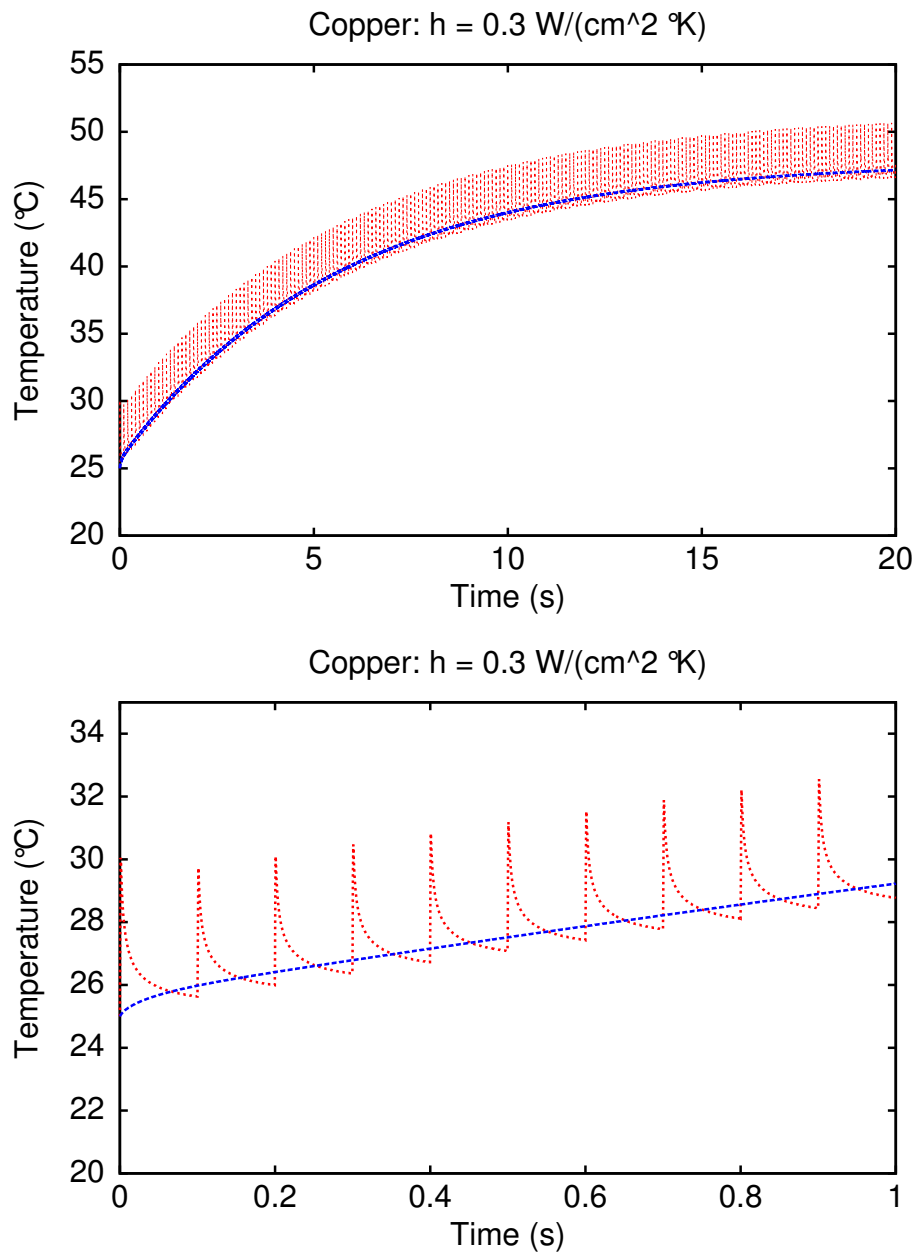
Figure 37: Transition of inner surface temperature from initial room temperature to steady-state oscillations for a copper collimator. The lower figure is an enlarged part of the upper figure.

6 Survival of Collimator Material in Emergency Case

Two materials, copper and titanium, were considered and compared as possible candidates for the collimators. In order to accomplish the goal of machine protection against off-energy and mis-steered bunches, the design of the collimators must include considerations of collimator damage at direct impacts of complete bunches.

In the case of an emergency, a fast safety system can send a signal to the RF gun and interrupt the bunch train during a time delay of $(2-3)\,\mu s$. This time defines the number of bunches from the train which can directly impact the collimator. The maximum number of dumped bunches can reach $M_b \simeq 30$, see table 4.

Why or how does a collimator fail? Usually the following reasoning is considered, based on the material properties from which the collimator is made: failure due to a rapid heating of the material when an instantaneous temperature rise creates thermal stresses which exceed the stress limits for a given material[15]. The principal mechanism for the damage is assumed to be an instantaneous energy deposition in the material due to the passage of high-energy and high-intensity particles.

---

[15]Later on we will refer to it as a thermal stress criterion, and the instantaneous temperature rise which will cause a collimator to fail, as a thermal stress limit.

Table 4: Number of bunches, M_b, which can be dumped in the collimator in the emergency case.

Bunch repetition rate, f_b, MHz	Bunch spacing Δt_b, μs	Number of bunches, M_b, in $\Delta t = (2-3)\,\mu s$
1	1.000	2 - 3
2	0.500	4 - 6
4	0.250	8 - 12
9	0.111	18 - 27

6.1 Instantaneous Heating and Collimator Damage

It is not simple to answer the question which heat load (or the number of bunches) the collimator may withstand without being damaged.

One of the first necessary steps is to establish a failure criteria for the collimators, since either yielding or fracture may prevent the satisfactory operation of the component. For collimators the actual usage of the material is of importance. For example, in tests with copper coupons and with high-intensity beams having small spot sizes (as at the collimators in linear colliders), it was found that even when the instantaneous heating was much larger than the analytical estimates would indicate, the damage was typically be confined to a region of a few times the beam core, and that no extensive cracks were seen [9]. Thus the process by which the collimator will fail has to be defined. The yield strength of the material is usually smaller than the ultimate strength, so the failure criterion based on the yield strength is more conservative and safe. For the collimators the failure criterion based on the ultimate tensile strength is often used [10], [11], [12], [13], [14]: the failure is caused by micro-fractures, at large temperature rise they may reach a critical size and cause unstable fracture of the material. Due to the fact that it is very difficult to obtain accurate and comprehensive data of the material failure in the experiments, both criteria will probably give some uncertainty.

As well as damage due to occasional instantaneous heating by some bunches, the collimators must resist the damage due to material fatigue from continual thermal cycling which depends on the heat load on the collimators under normal operation condition. For copper the experiments have indicated that fatigue damage can occur at $\sim 6 \cdot 10^7$ cycles at $120 \pm 10\,K$ temperature rise [14]. In section 5 it was presented that in the copper collimator the rise from room temperature to the steady state temperature is around $25°$. This was obtained with the assumption that 2% of the average beam power are absorbed by one collimator only, which probably overestimates the temperature rise in the steady state regime. The fatigue damage is not so critical for the collimators as for the beam dumps, but has to be taken into account. In the study of the post-linac collimation system for the NLC it is assumed that the fatigue temperature limit is 10% of the damage limit by bunches [14]. So the stress criteria has to comprise a static and a fatigue strength analysis.

The instantaneous temperature rise in the collimator depends on the parameters of the impacting beam: the particle energy, the intensity and the

beam spot size at the collimator, which we do not know exactly in the case of a machine failure. We could also not say how many bunches will be dumped in each collimator during the delay time, either the maximum number or the bunches may be distributed between different collimators, and what area on the surface will be hit. For the energy collimators, in the case of a fast energy error (for example, klystron phase errors, which are the most probable fast failure modes for the linear accelerators), we can expect the variation of a bunch-to-bunch energy, and hence the sweeping of bunches over some area on the energy collimator surface due to dispersion. Besides that due to different aperture radii and values of dispersion the energy collimators pick up the particles with different energy deviations: the first CE1 collimator takes the particles with large energy offsets of $|\Delta E/E_0| > 11\%$, and the second CE2 collimator mainly the particles with an energy deviation of $|\Delta E/E_0| < 10\%$ (see figures 13-14 and 18-19). A detailed analysis of all possible failure modes of the total linac and beam dynamics studies are required to understand these and others points.

As concerning the stress analysis, at present there are no analytical methods for determining with high precision the instantaneous temperature rise, which will cause a collimator made from a given material to fail, since the number of significant unknowns in the problem is large. The best way is the experimental tests of a chosen material under similar conditions. It is possible to perform a numerical calculation of the resulting stresses with temperature input from the thermal analysis (the ANSYS finite element code, for example) and compare the results with the stress limits, or to use some analytical estimates of the allowed temperature rise using the yield and tensile strengths taken from literature. Since the values of the yield and tensile strengths for pure materials and theirs alloys depend on the actual usage of the material and vary over a wide range [15], this will give uncertainties associated with the mechanical properties of the material.

Despite of many unknowns, for our purpose of comparing and selecting the material, we can make a rough estimate of the material survival using a simple approach which is often used in the first steps in the design in order to prevent failures. Taking into account the above mentioned uncertainties, the obtained estimates can be used only as a general indicator of the suitability of a material and the riskness of its installation. The approach used is described in the following steps.

- The design parameters of the beam were taken from table 1. Some

66

set of energies was considered taking in mind the different operation regimes of the TTF2 linac.

- It was assumed that in the case of a short (in comparison with the characteristic thermal conductivity time[16]) impact of electron bunches the instantaneous heating can be obtained from the enthalpy reserve of a given mass of the material and the calculated energy-deposition density [17].

- Thermal stress limits for both prospective collimator materials were estimated using a simple analytical formula for the induced static thermal stresses of a longitudinally and radially constrained cylinder [16] and the ultimate tensile strength of the material as a maximum allowed stress:

$$\Delta T_{stress} = \frac{2(1-\nu)\sigma_{ult}}{\alpha E_y} \ . \tag{18}$$

  The notations and material data used [17], [18], [19], [20] are listed in table 5. The obtained values were compared with the values which are reported and used in analogous studies [9], [10], [13], [14] and some typical values were taken as thermal stress limits, see table 5. The corresponding maximum allowable change in enthalpy was calculated taking into account the dependence of the specific heat on the temperature.

- The interaction between the beam and the material was modelled using the EGS4 code, and the energy-deposition density in both materials was calculated from a single bunch for different cases.

- Comparing the calculated energy-deposition density from a single bunch and the maximum allowable change in enthalpy, an estimate of the maximum number of bunches for a direct impact can be obtained for which the collimator material will be below the used thermal stress limit (not taking into account the possible cooling between successive bunches).

---

[16]The deposited heat is spread transversally through the heated area with the characteristic thermal conductivity time of $\tau_{dif} = \sigma_{x,y}^2 \cdot (\rho C_p)/k$, which is in our case $4\,\mu s \dots 25\,ms$ for the considered materials (copper and titanium) and the expected beam spot sizes of $\sigma_{x,y} = (20 - 500)\,\mu m$ (for the notations see in table 5), that is longer in most cases than the heating time of $(2-3)\,\mu s$.

It means also that the obtained estimates are valid for the case when all bunches impact and hit the same area on the collimator surface.

6.2   Beam Energy Deposition

The EGS4 shower code [4] was used for the calculation of the energy-deposition density in the material. In this section we briefly discuss the setup for the numerical calculations and the quality behaviour of the energy-deposition density for the TTF2 parameters.

The bunch was modeled by a Gaussian distribution in the standard 6-dimensional phase space $(x, p_x, y, p_y, z, \Delta E/E_0)$ to take into account the effect of the dispersion for the energy collimators. Since the TTF2 operation with various output energies is proposed, some set of the beam energy was taken, and the beam spot size of the impacting beam was varied in correspondence to the energy and the collimator location (the optical functions are different at the collimators). A sample of 10^6 particles was simulated for each case (the fluctuations in the energy deposition can practically not be seen for this number), and the energy deposition was scaled to the nominal bunch occupancy.

For the study of the material properties at the design TTF2 parameters, a block of the material has been taken with a length of 7.12 cm, which corresponds to two radiation lengths of titanium. The x and y dimensions of the block were large $(20\,cm)$ to allow the electromagnetic shower to develop fully. The main sensitive volume for the energy deposition recording was defined to be a box with x, y dimensions respectively of σ_x, σ_y, which correspond to the rms parameters of the impacting bunch. The longitudinal dimension of the box was defined to have approximately all three dimensions of the box equal (the 7.12 cm block were divided into $n_z = (100 - 500)$ slices). That means that all three dimensions of the box were varied with the bunch parameters. These boxes of equal volume are located along the z-axis, and in this way the maximum energy-deposition density close to the beam axis is determined as a function of the longitudinal position in the block. Besides this the chosen number of surrounding boxes (of the same volume as a main box) can be defined in both transverse directions to record the energy deposition as a function of the transverse positions (usually $n_{x,y} = 100$ was used).

Figure 38 shows an example of the distribution of the energy-deposition density in a copper block as a function of the longitudinal and transverse

Table 5: Relevant properties and thermal damage parameters of two prospective collimator materials used in this study. The melting limit is also presented for the comparison: $\Delta T_{melt} = T_{melt} - T_{room}$, $T_{room} = 25°C$.

	Cu	Ti	Symbol	Units
Z	29	22	Z	
Atomic weight	63.55	47.88	A	
Density	8.96	4.54	ρ	g/cm^3
Specific heat	0.385	0.525	C_p	$J/(gK)$
Thermal conductivity	4.01	0.219	k	$W/(cmK)$
Melting point	1080	1670	T_{melt}	$°C$
Radiation length	1.43	3.56	L_R	cm
Stopping power	12.8	7.2	dE/dz_{min}	MeV/cm
Critical energy	18.8	25.0	E_c	MeV
Coeff. of thermal linear expansion	16.5	8.5	α	$10^{-6}/K$
Young's modulus	120	110	E_y	GPa
Tensile strength	300	330-600	σ_{ult}	MPa
Poisson ratio	0.34	0.33	ν	-
Velocity of sound	3.66	4.92	$c_s = \sqrt{\frac{E_y}{\rho}}$	$10^5\,cm/s$
Stress limit (18)	200	470-850	ΔT_{stress}	K
$C_p =$				
$a+$	0.358	0.459	a	$J/(gK)$
$bT+$	$9.63 \cdot 10^{-5}$	$2.20 \cdot 10^{-4}$	b	$J/(gK^2)$
dT^{-2}	0	0	d	
Maximum allowed temperature rise: ΔT_{max}				
Stress limit	180	770	ΔT_{stress}	K
Melting limit	1055	1645	ΔT_{melt}	K
Maximum allowable change in enthalpy: ΔH_{max}				
Stress limit	71	469	ΔH_{stress}	J/g
Melting limit	462	1062	ΔH_{melt}	J/g

positions. Figure 39 presents a comparison of the development of the electromagnetic shower in the copper and titanium blocks at the same conditions. Simulation studies have shown that for both materials in the energy range of $E_0 \in [0.3, 1.0]\, GeV$:

- The shower maximum (the maximum of the energy-deposition density) occurs in the first few millimiters from the material surface (the position of the maximum is slightly changed with the variation of the beam spot size).

- The shower propagates for $\sim 2\, cm$ along the axis and essentially reduces at the depth of $\sim 3\, cm$ from the material surface.

- The maximum value of the energy-deposition density is defined mainly by the beam spot size (and by the beam intensity which was fixed) and depends only slightly on the beam energy (at the same beam spot sizes) and on the material type.

6.3 Survival of Collimator Material

We have four collimators in each collimator location scheme. The $\beta-$functions in the locations of the two transverse collimators, CT1 and CT2, are large enough in both schemes: $\beta_{x,y} \in [10, 30]\, m$. The energy collimators, CE1 and CE2, are placed in the dogleg where the $\beta-$functions are small: $\beta_{x,y} \in [0.5, 5]\, m$. The worst case is the first energy collimator, at the entrance of which the beam spot size at $1\, GeV$ energy is $\sqrt{\sigma_x \sigma_y} \simeq 50\, \mu m$ taking into account the energy spread in the bunch.

The energy-deposition density from a single bunch in both materials, titanium and copper, have been calculated for all collimators and for both collimator location schemes. The following simulation procedure was used. The Gaussian distribution of particles was generated at the collimator section entrance for different cases according the setup described in the previous section. This distribution was tracked to each collimator using the TrackFMN code. The output distributions were picked up by the EGS4 code and fired into the block of the material using the setup described. The maximum value of the energy-deposition density for each case was used for the estimation of the number of bunches, N_b, at which the collimator material will still be below the thermal stress limit. The obtained estimates, averaged over
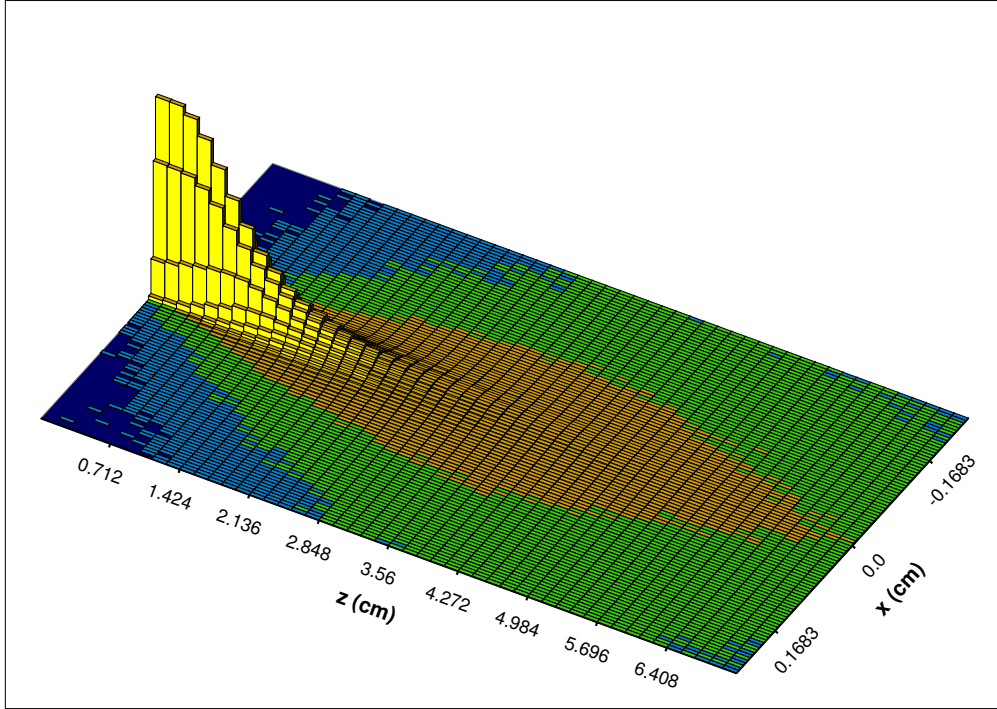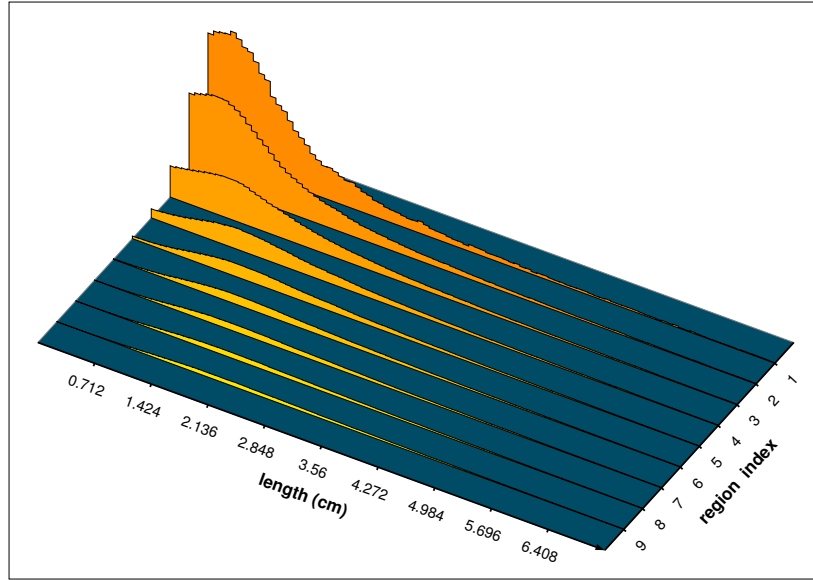
70

Figure 38: Energy-deposition density in the copper block as a function of longitudinal and transverse positions. The particles of the incident beam have 1 GeV energy. The beam spot size is given by $\sqrt{\sigma_x \sigma_y} \simeq 50\,\mu m$ (the case of the CE1 collimator). The different colors mark the different values of the energy-deposition density.
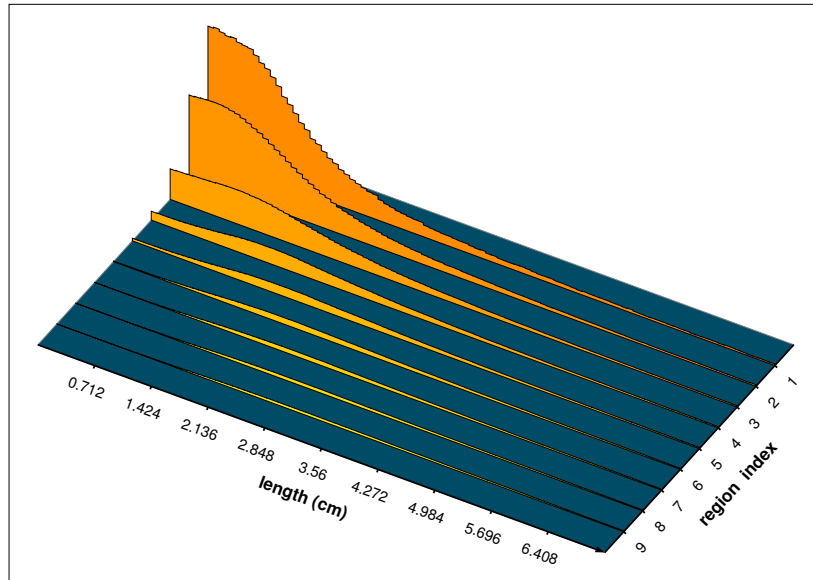
71

Figure 39: Energy-deposition density in the copper (top) and titanium (bottom) blocks as a function of longitudinal and transverse positions. The particles of the incident beam have an energy of $1\,GeV$. The beam spot size is given by $\sqrt{\sigma_x \sigma_y} \simeq 50\,\mu m$ (the case of the CE1 collimator). A region index marks a number of the recording box starting from the beam axis: index 1 corresponds to the main box.

72

the two collimator location schemes and for all transverse collimators, are summerized in table 6. As an illustration, figure 40 shows a comparison of the melting limit, the thermal stress limit and the behaviour of the energy-deposition density (for the main recording boxes as the maximum value in the radial direction) in the copper block from 30 bunches as a function of the longitudinal position.

It must be noted here, remembering all above mentioned uncertainties in the problem of the material survival, that these numbers, obtained with the help of the simple analytical approach, give us the information about the relative behaviour of two prospective materials for the collimators and of each collimator in the collimator section. The absolute numbers can be used only as a very rough estimate. What may we conclude keeping in mind that the maximum number of bunches, which can be dumped in each collimator, may reach $M_b \sim 30$ and taking into account the possible operation regimes of the TTF2 linac?

- All collimators made from titanium show good survival properties for the design TTF2 parameters.

- Collimators CT1 and CT2 made from copper, probably, will also be suitable. In the future for collimator location scheme 2 one may hope to increase the $\beta-$functions at the CT1 and CT2 locations, since they are placed in the straight section after the accelerating modules, where some possibility to change the optical functions exists.

- For the operation at the maximum energy of $1\,GeV$ and with the bunch frequency of $9\,MHz$ there will be a problem with the material survival of the CE1 and CE2 collimators made from copper. The worst case is expected for the CE1 collimator[17].

- For the first operation of the TTF2 at an energy $E_0 < 0.5\,GeV$ and with $f_b \simeq 2\,MHz$ the CE1 and CE2 collimators made from copper may be below the thermal stress limit.

---

[17]Note here once more, that the discussed estimates do not take into account the sweeping of bunches with different energies over the collimator surface due to dispersion.

Table 6: Rough estimates of the maximum number of bunches, N_b, for which the collimator materials are below the thermal stress limits used in these studies.

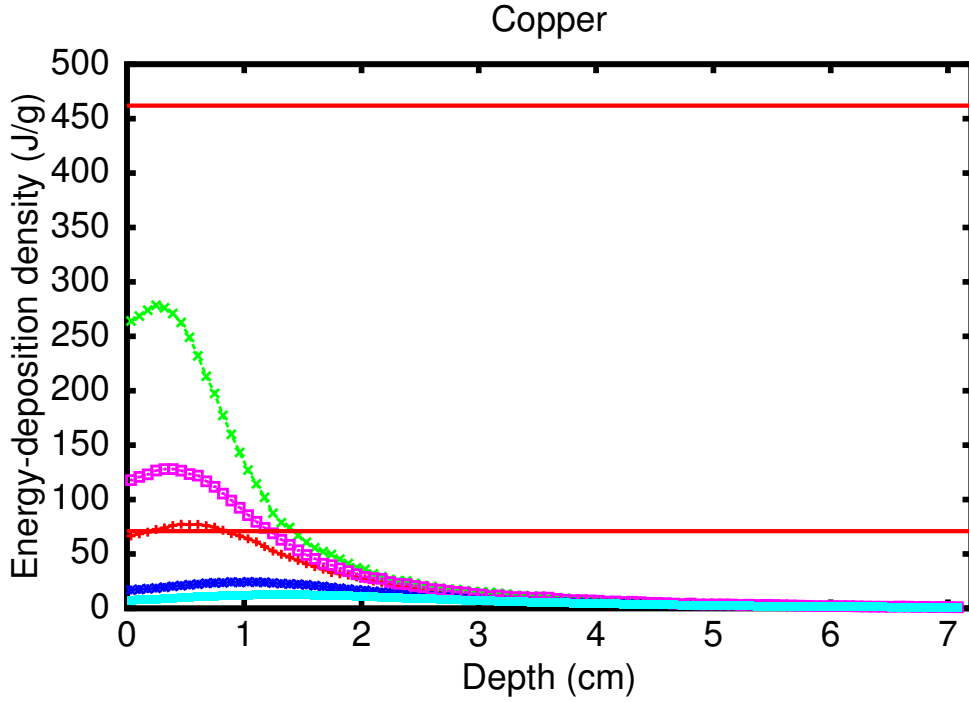| Name of collimator	**Cu** $\Delta T_{stress} = 180°$		**Ti** $\Delta T_{stress} = 770°$	
	$0.6\,GeV$	$1.0\,GeV$	$0.6\,GeV$	$1.0\,GeV$
CT1, CT2	~ 67	~ 40	~ 280	
CE1	~ 12	~ 8	~ 75	~ 53
CE2*	~ 22	~ 14	~ 135	~ 95

Figure 40: Energy-deposition density in the copper block from 30 bunches as a function of the longitudinal position. The particle energy is $1\,GeV$. The different curves correspond to different initial beam spot sizes: $\sigma_x \times \sigma_y = 50 \times 50$, 75×75, 100×100, 200×200, $300 \times 300\,\mu m^2$ (from upper to lower). The melting (upper) and thermal stress (lower) limits are shown by straight lines.

7 Summary

The main purpose of this study was to find a collimation scenario for the protection of the undulators which will be installed at the TESLA Test Facility phase 2. Being limited in the possibilities to create an optics most suitable for collimation, we have looked over all free places as candidates for the collimator location and as a result found two, as it seems, most promising schemes of collimator placement (scheme 1 and scheme 2 in the notation of this paper). After that these two schemes were carefully compared from different points of view and the collimator location scheme 2 with collimators manufactured from copper was selected as recommendation for practical realization. This scheme has a few critical points and its advantages can be understood mainly in the comparison with other possible collimation scenarios. Some of its critical points and questions open for further research were already pointed out in the text and some are shortly listed below.

- Three out of four collimators have aperture radii of $2\,mm$ and, nevertheless, even being small these values are still so close to the border of the set of protecting apertures, that alignment errors, if considered without correction, lead to a noticeable degradation of the collimation quality. Thus further detailed studies of correction algorithms, which will help to restore the collimation quality as much as possible, is needed.

- Wakefields produced by small collimator apertures may result in an unacceptable degradation of the main beam quality. This question was not seriously studied yet, but the decision was made to manufacture collimators as blocks of material with several holes [21], the radius of which increases from the minimum aperture ($2\,mm$) to the full aperture of the vacuum chamber (collimator is open). Such design, as we hope, will give the possibility to find some compromise between the undulator protection requirement and the wakefield dilution of the beam emittance. It also gives us a lot of new problems (theoretical and experimental) for investigations.

- The survival of the energy collimators made from copper at the design TTF2 parameters is a crucial point. Further accurate and detailed studies of all possible failure modes of the total machine are needed to investigate the probability of direct impacts of some bunches in these

collimators and of the bunch sweeping over the collimator surface. For the future the collimators made from other materials: titanium, combined materials (titanium and copper) and others, can be considered.

8 Acknowledgements

References

[1] H. Schlarb, *Collimation System for the VUV-FEL at TTF*, DESY Thesis-2001-055, November 2001.

[2] M. Dohlus and R. Wanzenberg, *Unpublished note.*

[3] V. Balandin, *The TrackFMN Program. User's Reference Manual*, Unpublished.

[4] W.R. Nelson, H. Hirayma, and D.W.O. Rogers, *The EGS4 code system*, SLAC Report 265 (1985).

[5] R.M. Besancon (editor), *The encyclopedia of Physics*, New York: Reinhold, 1966.

[6] I.S. Baishev, M.A. Maslov, and M. Seidel, *Design Study of a Beam Dump for the TESLA and S-Band Test Facilities at DESY*, DESY TESLA 95-10.

[7] Allan W. Scott, *Cooling of Electronic Equipment*, JON WILEY & SONS.

[8] V. Balandin, *Private communication.*

[9] M.C. Ross, R. Iverson, K. Jobe, D. McCormick, P. Tenenbaum, and P. Raimondi, *Single Pulse Damage in Copper*, Proc. of the 20th International Linac Conference, Monterey, California, 21-25 Aug 2000, vol.1, p.47-49.

[10] NCL Design Group, *Zeroth-Order Design Report for the Next Linear Collider. Collimation Systems*, pp.556-642, 1996.

[11] R. Brinkmann, A. Drozhdin, D. Schulte, and M. Seidel, *The TESLA Beam Collimation System*, DESY TESLA 95-25.

[12] R. Brinkmann, N.J. Walker, and G.A. Blair, *The TESLA Post-linac Collimation System*, TESLA Report 2001-12.

[13] W.R.Nelson, S.H.Rokni, and V.Vylet, *Radiation calculation and shielding considerations for the design of the next linear collider*, SLAC-PUB-7336, 1996.

[14] NCL Post-Linac Collimation Task Force, *New Post-Linac Collimation System for the Next Linear Collider*, LCC-Note-0052.

[15] http://www.efunda.com/materials/

[16] P. Sievers. *Elastic stress waves in matter due to rapid heating by an intense high-energy particle beam*, LAB.II/BT/74-2, June 1974.

[17] A.N.Kalinovskii, N.V.Mokhov, and Yu.P.Nikitin, *Passage of High-Energy Particles through Matter*, AIP, New York, 1989.

[18] R.H.Perry and C.H.Chilton (editors), *Chemical Engineers' Handbook*, McGraw-Hill Book Company.

[19] David R. Lide (Editor-in-Chif), *CRC Handbook of Chemistry and Physics*, CRC Press, 1999-2000.

[20] Vsevolod V. Balashov, *Interaction of Particles and radiation with Matter*, Springer 1997.

[21] Manfred Rüter, *Private communication.*